



High-surface-area zinc aluminate supported silver catalysts for low-temperature SCR of NO with ethanol

Aurélien Flura, Fabien Can*, Xavier Courtois, Sébastien Royer, Daniel Duprez

Université de Poitiers – Institut de Chimie des Milieux et des Matériaux de Poitiers – IC2MP UMR 7285 CNRS, 4 Rue Michel Brunet – Bât. B27, 86022 Poitiers Cedex, France

ARTICLE INFO

Article history:

Received 29 March 2012

Received in revised form 9 July 2012

Accepted 16 July 2012

Available online 23 July 2012

Keywords:

Ag/Zn–Al₂O₃

Ethanol

SCR

NO_x

NH₃

ABSTRACT

The NO_x selective catalytic reduction of ethanol (EtOH-SCR) was studied using a complex gas mixture representative of a diesel exhaust, over zinc alumina mixed oxide supported silver catalysts (2 wt.% Ag/Zn_x–Al₂O₃, with $x = 10\text{--}20\text{--}33$ at.%). The supports were obtained using a template assisted sol–gel route in order to achieve high surface areas. For the higher Zn loading (33%), the calcination temperature has been raised from 600 °C to 800 °C then 1000 °C in order to evaluate thermal stability of these materials. Addition of zinc in alumina network leads to the formation of the spinel-type zinc aluminate structure. Chemical and physical characterizations of the catalysts have been confronted with the EtOH-SCR results, in order to understand the respective influence of the metal and support in nitrogen formation. This study shows that addition of zinc and modification of the support calcination temperature both play upon the Lewis acidic sites (LAS) concentration and density, determined by pyridine adsorption monitored by FTIR spectroscopy. This parameter is shown to be related with ammonia emission at $T \geq 350$ °C. Besides, formation of nitrogen at $T \leq 350$ °C is shown to be dependent on (i) the rate of acetaldehyde formation and (ii) the reactivity of acetaldehyde in SCR of NO reaction. Modification of the alumina support directly impacts these parameters. Finally, it is demonstrated that Zn is a hopeful candidate to increase the EtOH-SCR activity at low temperature ($T \leq 300$ °C).

© 2012 Elsevier B.V. All rights reserved.

1. Introduction

The current environmental legislations lead to increase the interest in Diesel engines technology from automobile manufacturers. Compared to gasoline engines, Diesel engines work in lean-burn conditions, which lead to decrease the carbon dioxide emissions. However, NO_x (NO + NO₂) contained in Diesel exhaust gas, i.e. in oxidizing atmosphere, is hardly reduced into N₂ using a conventional three-way catalyst (TWC). Among the processes effective to reduce NO_x in lean condition, two technologies are usually proposed in the literature: (i) the NO_x storage–reduction (NSR) concept [1], working in transient conditions; and (ii) the selective catalytic reduction (SCR). The SCR is described as a promising way to reduce NO_x, with the possible use of a large choice of reducers including unburned hydrocarbons, urea, ammonia, hydrogen or alcohol for instance. Actually, under the impulse of environmental legislation, the urea-CR process is considered as a possible technological issue to reduce NO_x from light vehicles, as reported in numerous publications [1–10]. This technology, usually applied for the NO_x reduction from stationary sources, meet however some drawbacks to be transposed in NO_x reduction of Diesel engines.

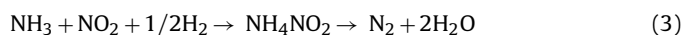
First, even if the decomposition of the liquid urea solution (used as ammonia precursor) has been studied in the literature, urea hydrolysis is rather complex and not well understood yet. For instance, it was reported that in similar conditions, catalytic performances obtained with urea solution are largely lower than those obtained using ammonia [11]. Secondly, the thermal stability of zeolite exchanged transition metal (Cu, Fe), proposed for this application [12–14] in association with a Diesel particulates filter, does not seem to be fully mastered yet.

Hydrocarbon-SCR has been largely studied as well [15–23]. Recently, alumina supported silver catalysts (Ag/Al₂O₃) have taken particular interest [24–26], especially due to their reactivity toward oxygenated compounds. For instance, ethanol has been reported as an attractive reducer for the SCR reaction. Miyadera [27] showed that Ag/Al₂O₃ catalyst is able to reduce NO_x with ethanol in lean-burn conditions, from temperature as low as 250 °C. Compared to urea-CR, the use of ethanol as a reducer agent can be justified by the existence of an ethanol-based fuel (such as E85) distribution network in numerous countries. Thereby, EtOH-SCR with mobile engine could easily be performed using a specific tank even if it would require an extra injector in the exhaust pipe, placed before the catalyst (same problem as urea addition, but ethanol is by far less corrosive). In addition, ethanol is a particularly attractive reducer candidate for NO_x removal because it is environmentally relatively benign.

* Corresponding author. Tel.: +33 0 549453997; fax: +33 0 549453741.

E-mail address: fabien.can@univ-poitiers.fr (F. Can).

Numerous studies were conducted to understand the mechanism of NO_x reduction by ethanol, together with the role of silver [28–33] and alumina [34–36] in nitrogen selectivity. Nevertheless, if the mechanisms of NO_x reduction with oxygenates compound have been extensively studied, unfortunately, among the more quoted papers [37–39], none directly focus on the reaction selectivity, especially toward NH_3 emission. In fact, the proposed mechanisms suggest the transformation of ethanol in surface acetate ions or enolic surface species [38], that furthermore react with NO_2 to produce nitromethane which is finally transformed in isocyanate species ($-\text{NCO}$, reaction (1)). The formation of $-\text{NCO}$ species over $\text{Ag}/\text{Al}_2\text{O}_3$ catalysts is reported in numerous papers when high NO_x reduction efficiency is achieved [40,41]. The chemistry of HNCO formation is well established [37,41] and involves hydrolysis of HNCO to form NH_3 , via reaction (2). Thereafter, ammonia is proposed to react with nitrous acid (HNO_2) to form ammonium nitrite. Ammonium nitrite is thermally unstable above 100°C , and easily decomposes into H_2O and N_2 (reaction (3)). Isocyanate ions can also react with NO_2 [37] at low temperature (e.g. below 200°C). This reaction is however slower than that of $-\text{NCO}$ with water which leads to ammonia formation.



Catalytic active sites of this multi-step reaction mechanism are still controversial and discussed. For instance, many studies deal on the relationship between the structural features of silver species and their catalytic behavior. It appears that ethanol SCR (EtOH-SCR) is catalyzed rather by oxidized silver cations (Ag^+) and/or oxidized silver clusters ($\text{Ag}_n^{\delta+}$) [42–46]. In parallel, metallic silver species was proposed as active in partial oxidation of hydrocarbon (*n*-dodecane or ethanol), which promote the SCR activity [47,48]. Then, an optimal ionic/metallic balance of silver species is proposed in the literature in order to produce efficient EtOH-SCR activity [49]. Also, surface properties of oxides supports are known to influence the dispersion of the chemical species on the catalyst. In particular, the alumina support has been shown to activate $\text{Ag}_n^{\delta+}$ clusters formation on its acid sites [50]. Alumina acidic and basic properties have been shown to play a crucial role in the SCR of NO_x with propane, using $\text{Ag}/\text{Al}_2\text{O}_3$ catalyst [36]. In fact, when ethanol is used as reducer, aluminum coordinatively unsaturated sites (CUS) have been recently reported as involved in NO_x abatement mechanism [51,52].

Finally, Diesel engine exhaust temperature commonly ranges from 200 to 250°C . However, studies of EtOH-SCR with $\text{Ag}/\text{Al}_2\text{O}_3$ catalysts show that the system activity is limited below 350°C . The challenge in EtOH-SCR over $\text{Ag}/\text{Al}_2\text{O}_3$ is then to decrease the working temperature of the catalyst. For instance, Zhang et al. [53] have shown that addition of H_2 in the gas mixture, upstream of the catalyst, greatly enhanced the nitrogen formation at $T \leq 350^\circ\text{C}$. However, it implies to introduce or produce H_2 on-board.

The objective of this work is to present another alternative to enhance SCR activity at low temperature, i.e. below 350°C . Working over Ag-based catalyst, the alumina support was modified by zinc introduction. The effects of (i) Zn content and (ii) the sample calcination temperature have been investigated over the alumina-substituted structure, in order to increase the catalytic activity. Silver content is fixed to 2.0 wt.%, since it has been largely reported in the literature as the optimum loading in EtOH-SCR [27,54,55]. Catalysts have been characterized by nitrogen physisorption, X-ray diffraction, transmission electron microscopy, diffuse-reflectance UV–visible, H_2 -temperature programmed reduction and Fourier

transformed infrared spectroscopy of adsorbed pyridine and CO_2 , in order to identify active sites.

2. Experimental

2.1. Catalysts synthesis

The alumina support was prepared according to an optimized template-assisted sol–gel synthesis route [56]. The aluminum precursor (aluminum sec-butoxide, 97% Alfa Aesar) was dissolved in 1-butanol at 65°C , and mechanically stirred until complete dissolution. In parallel, the template [(1-hexadecyl) trimethylammonium, 98% Alfa Aesar] was dissolved in 1-butanol. The two solutions were then mixed under gentle stirring at 65°C . After a homogeneous solution is obtained, a limited amount of water was drop-wise added under vigorous stirring for hydrolysis. The molar composition of the mixture at this step was (in mol.%): $1\text{Al}^{3+}/0.5\text{CTABr}/10\text{ButOH}/2\text{H}_2\text{O}$. Stirring was thereafter maintained for 4 h at 65°C until homogeneity is obtained. The resulting gel was transferred into a Teflon-line autoclave for hydrothermal treatment at 100°C for 24 h. After cooling down to room temperature, the solid was recovered by filtration, extensive washing and drying at room temperature for 24 h. Before use for impregnation, the solid was calcined under synthetic dry air at 600°C for 4 h (temperature increase rate = $3^\circ\text{C}/\text{min}$).

The Zn-loaded aluminas supports were synthesized using the same *modus operandi* as described above, except that the zinc precursor ($\text{Zn}(\text{NO}_3)_2 \cdot 6\text{H}_2\text{O}$, 98% Sigma–Aldrich) was dissolved in the hydrolysis solution. To ensure a complete dissolution of the precursor, the calculated weight (to achieve the desired Zn-content in the alumina) was dissolved in a hot mixture of 1-butanol and water, which was used, after cooling, as hydrolysis solution. The three Zn-containing alumina supports were synthesized at $\text{Zn}/(\text{Al} + \text{Zn})$ atomic ratio of 0.1, 0.2 and 0.33. The supports are named $\text{Zn}_{0.1}\text{-Al}_2\text{O}_3$, $\text{Zn}_{0.2}\text{-Al}_2\text{O}_3$ and $\text{Zn}_{0.33}\text{-Al}_2\text{O}_3$, respectively. In addition, the influence of the calcination temperature on the catalyst properties was studied for the $\text{Zn}_{0.33}\text{-Al}_2\text{O}_3$ support. So the $\text{Zn}_{0.33}\text{-Al}_2\text{O}_3$ support was calcined at 800°C ($\text{Zn}_{0.33}\text{-Al}_2\text{O}_3$ C800) then 1000°C ($\text{Zn}_{0.33}\text{-Al}_2\text{O}_3$ C1000), using the same program ($3^\circ\text{C}/\text{min}$, kept 4 h before cooling). Table 1 reports the zinc atomic content and the calcination temperature of the different alumina-based supports used in this study.

The Ag impregnation procedure (always at 2 wt.% Ag^0) was inspired by the work of Sato et al. [57], using ethanol as solvent. Authors showed that using ethanol instead of water as solvent leads to better EtOH-SCR results, due to an enhancement of the silver particles dispersion. The Ag impregnation was carried out as follow: 980 mg of alumina (or Zn-loaded alumina) was crushed (granules diameter < $100\ \mu\text{m}$), and was added to 28 mL of ethanol stirred at room temperature. Two milliliters of an aqueous solution of AgNO_3 (>99%, Sigma–Aldrich – $[\text{AgNO}_3] = 9.27\ \text{mol/L}$) was slowly added, and stirring was maintained for 30 min. The impregnated solid was then heated at 80°C for 150 min. Thereafter, the product was recovered by filtration, washed with ethanol, and dried in oven at 120°C during 16 h. Finally, all catalysts were calcined under synthetic air containing 10 vol.% of water (600°C for 4 h, temperature increase rate = $3^\circ\text{C}/\text{min}$). The effective Ag content was measured by ICP, and it is always ranging from 1.91 wt.% to 1.95 wt.%.

2.2. Physical and structural characterization

Nitrogen adsorption–desorption isotherms were recorded at -196°C , using a Tristar 3000 Micromeritics apparatus. Prior to the measurement, the samples were pretreated at 250°C under vacuum for 5 h. The surface area was calculated using the BET model,

the pore volume is evaluated at $P/P_0 = 0.97$, and the pore diameter was measured by using the BJH model applied to the desorption branch of the isotherms.

Catalysts were characterized by powder X-ray diffraction using a Bruker D5005 diffractometer equipped with a monochromatized $\text{CuK}\alpha$ radiation ($\lambda = 1.5418 \text{ \AA}$) operated at 40 kV and 30 mA. The diffraction patterns were recorded in the 2θ value range $15\text{--}75^\circ$, with a step of $0.04^\circ \text{ s}^{-1}$ and a step time of 6 s. Crystalline phases were identified by comparison with ICDD database files. The crystallite size were calculated using Scherrer equation: $D_{hkl} = K\lambda/\beta \cos \theta$, where K = structure constant (0.9 for spherical crystals); λ = incident ray wavelength (0.15418 nm); β = peak width at half height after correction for instrumental broadening (rad), θ = Bragg angle. In addition, the crystallite size was also estimated considering the Rietveld formalism.

Transmission electron microscopy (TEM) micrographs were recorded on JEOL 2100 instrument (operated at 200 kV with a LaB_6 source and equipped with a Gatan Ultra scan camera). EDX spectroscopy was carried out with a Hypernine (Premium) detector (active area: 30 mm^2) using the software SM-JED 2300T for data acquisition and treatment. EDX analysis zone was defined on the particle, and it was generally ranging from 5 to 15 nm.

Diffuse reflectance UV–vis spectra were recorded at room temperature between 200 nm and 500 nm on a Varian Cary 5000 spectrometer equipped with a double monochromator. BaSO_4 was used as reference. Considering the strong absorbance of the alumina-based supports, the spectrum of bare oxides ($\text{Zn}_x\text{-Al}_2\text{O}_3$, with $x = 0\text{--}10\text{--}20\text{--}33 \text{ at.}\%$) was subtracted from silver catalyst to focus on the silver species contribution.

2.3. Surface properties

The surface acidity of the Ag-impregnated materials was evaluated by IR spectroscopy of adsorbed pyridine. IR spectra were collected with a Nexus Nicolet spectrometer equipped with a DTGS detector (Deuterium TriGlyceride Sulfur) and KBr beam splitter. IR spectra were recorded with a resolution of 4 cm^{-1} and 64 scans. The presented spectra were normalized to a disc of 10 mg/cm^2 . After activation at 450°C , pyridine was adsorbed (200 Pa at equilibrium) at room temperature. Desorption was performed up to 450°C , by temperature step of 50°C . The ν_{8a} spectral region was deconvoluted using the peak resolve function of the Omnic software, that allows obtaining the amount of tetrahedral Al^{3+} (strong Lewis acid sites – LAS) and both tetrahedral Al^{3+} and an octahedral Al^{3+} (medium to weak LAS). The total amount of LAS was determined from the area of the ν_{19b} band, using its molar coefficient ($\epsilon_{\nu_{19b}} = 1.5 \text{ cm}^2 \text{ mol}^{-1}$ [58]).

2.4. Redox properties

Temperature programmed reduction (TPR) experiments were performed on an Autochem 2920 Micromeritics apparatus equipped with a thermal conductivity detector (TCD). Sample of

about 150 mg was placed in a U-shape quartz reactor. Prior to the TPR measurements, the sample was calcined at 550°C under 10 vol.% O_2 in Ar flow (temperature increase rate = 10°C/min – step time = 1 h). The sample was cooled down to room temperature, and it was purged under Ar flow. The reduction was carried out under 1 vol.% H_2 in Ar flow up to 800°C (temperature increase rate = 5°C/min). TCD signal being sensible to water, an H_2O -trap was added downstream of the reactor, allowing the quantification of the H_2 consumed during the TPR experiment.

2.5. Catalytic activity measurements

Catalytic tests were performed in a quartz tubular micro-reactor under a flow simulating realistic Diesel engine exhaust conditions (flow composition: 400 ppm NO, 500 ppm CO, 167 ppm H_2 , 1200 ppm $\text{C}_2\text{H}_5\text{OH}$, 8% O_2 , 10% H_2O and 10% CO_2 balanced in N_2). Gas flows were controlled using mass-flow controllers (Brooks), except for H_2O and $\text{C}_2\text{H}_5\text{OH}$ which were introduced using thermostated saturators. The gas hour space velocity (GHSV, calculated as the volume of feed gas/volume of the catalyst content) was fixed at $150,000 \text{ h}^{-1}$. For each studied temperature (150°C , 250°C , 300°C , 350°C , 450°C and 550°C), the activity of the catalysts was followed until stabilization.

Prior to the analyzers, H_2O was removed in a condenser cooled at 0°C . Both NO and NO_x concentrations ($\text{NO} + \text{NO}_2$) are measured by chemiluminescence (Monitor Europe ML9841AS); CO and N_2O are quantified by FTIR analyzers (COSMA Beryl 100). In addition, the outlet water was condensed for 30 min after stabilization of the activity. The effluent gas mixture passed through a condenser filled with 10 mL of demineralized water. NH_4^+ , NO_2^- and NO_3^- concentrations were determined by HPLC (Thermo Finnigan, equipped with an Alltech Universal Cation column $7 \mu\text{m}$, $4.6 \text{ mm} \times 100 \text{ mm}$ for NH_4^+ ; and Agilent Eclipse XDB-C18, $5 \mu\text{m}$, $4.6 \text{ mm} \times 50 \text{ mm}$ for NO_2^- and NO_3^-). NO_2^- and NO_3^- were added to the unconverted NO_x . NH_4^+ analysis was used to calculate the NH_3 selectivity.

Ethanol conversion, as well as CH_3CHO , CH_3OH , CH_2O , C_2H_4 and CH_4 formation, was measured using a Gas Chromatograph (Varian 3400, Supelco HaySep R, 60–80 mesh, $1/8' \times 2000 \text{ mm}$) equipped with a FID detector. The N_2 selectivity was calculated assuming no other N-compounds than NO, NO_2 , N_2O and NH_3 are formed. In order to validate the results, every outlet gas ($\text{C}_2\text{H}_5\text{OH}$, CH_3CHO , CH_3OH , CH_2O , C_2H_4 , CO, NO, NO_2 , NH_3 , N_2O) was regularly checked with an infrared detector (MKS MultiGas 2030 FT-IR).

3. Results

3.1. Physical properties

3.1.1. Textural properties

Table 1 summarizes the textural properties of the supports deduced from the N_2 adsorption/desorption isotherms.

Alumina support exhibits a high surface area ($263 \text{ m}^2/\text{g}$), even after thermal treatment at 600°C with a feed stream including

Table 1
Main characteristics and textural properties of the synthesized catalysts.

Catalysts	Zn/[Al + Zn] (at.%)	Support calcination $T(^{\circ}\text{C})$	S_{BET} (m^2/g)	V_t (cm^3/g)	D_p (nm)	Medium LAS ^a density ($\mu\text{mol}/\text{m}^2$)
Ag/ Al_2O_3	0	600	263	1.13	9.6	0.012
Ag/ $\text{Zn}_{0.1}\text{-Al}_2\text{O}_3$	10	600	205	0.38	5.9	0.018
Ag/ $\text{Zn}_{0.2}\text{-Al}_2\text{O}_3$	20	600	208	0.37	5.6	0.018
Ag/ $\text{Zn}_{0.33}\text{-Al}_2\text{O}_3$	33	600	154	0.37	7.3	0.025
Ag/ $\text{Zn}_{0.33}\text{-Al}_2\text{O}_3$ C800	33	800	117	0.32	8.0	0.016
Ag/ $\text{Zn}_{0.33}\text{-Al}_2\text{O}_3$ C1000	33	1000	65	0.16	8.6	0.009

V_t is the total pore volume at $P/P_0 = 0.97$; D_p is the pore diameter calculated from the desorption branch of the isotherm using the BJH method.

^a Integration of ν_{8a} band at 1617 cm^{-1} after pyridine evacuation at 450°C .

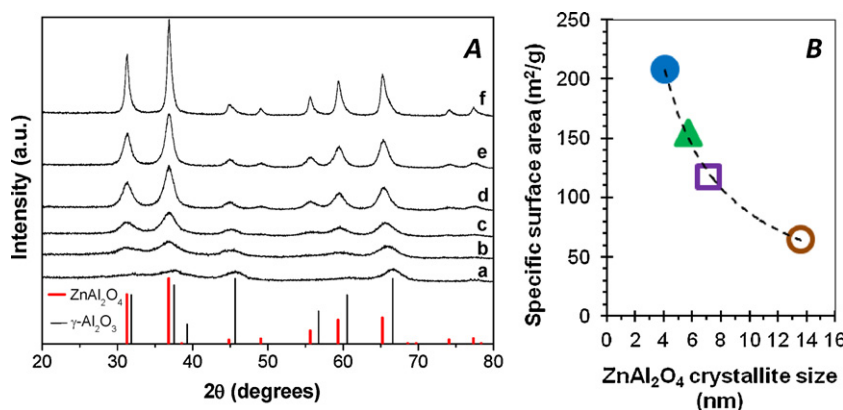


Fig. 1. (A) XRD patterns of silver supported catalysts. (a) Ag/Al₂O₃; (b) Ag/Zn_{0.1}-Al₂O₃; (c) Ag/Zn_{0.2}-Al₂O₃; (d) Ag/Zn_{0.33}-Al₂O₃; (e) Ag/Zn_{0.33}-Al₂O₃ C800; (f) Ag/Zn_{0.33}-Al₂O₃ C1000. (B) Relation between the surface area and the spinel crystallite size. (●) Ag/Zn_{0.2}-Al₂O₃; (▲) Ag/Zn_{0.33}-Al₂O₃; (□) Ag/Zn_{0.33}-Al₂O₃ C800; (○) Ag/Zn_{0.33}-Al₂O₃ C1000.

10 vol.% H₂O. A large pore diameter (9.6 nm) is also obtained. These two parameters are favorable for the dispersion of an active phase, and a use in gas phase reaction. The introduction of Zn²⁺ in substitution of Al³⁺ at 10 and 20 at.% leads to a decrease of the surface area of approximately 22% at 205–208 m²/g, associated with a decrease of the pore diameter down to 5.6–5.9 nm. A further increase in Zn loading (up to 33 at.% of Zn³⁺, given the ZnAl₂O₄ composition) results in an additional decrease in surface area, which falls to 154 m²/g, and a slight increase in pore diameter (7.3 nm).

The increase in calcination temperature for Zn_{0.33}-Al₂O₃ support up to 800 °C or 1000 °C, results in progressive increase in mean pore diameter and decrease in surface area. At 1000 °C, a surface area of 65 m²/g and a pore diameter of 86 nm are obtained, which is however consistent with a progressive increase in crystal/particle size increase during sintering phenomena. Then, Zn²⁺ substitution in the alumina structure, as well as the calcination temperature, influences the final textural properties of the material.

3.1.2. Structure properties

Crystallinity of the Ag/Zn_x-Al₂O₃ materials was studied by XRD. Fig. 1(A) shows the effect of zinc addition and calcination temperature on the structure of the materials. The Ag/Al₂O₃ material displays the classical γ-Al₂O₃ structure [ICDD PDF no. 00-050-0741(I)]. When Zn²⁺ is incorporated into the structure, ZnAl₂O₄ spinel-type structure reflections are observed [ICDD PDF no. 01-082-1535 (C)]. This phase is clearly observed from 10 at.% Zn²⁺, with the shift of the γ-Al₂O₃ reflections to the lower 2θ values. Nevertheless, we suppose an overlapping of the reflections of the ZnAl₂O₄ and the γ-Al₂O₃ structures until the 33 at.% of Zn²⁺ in alumina.

Whatever the Zn²⁺ content and the calcination temperature, Ag phase (either oxide or metallic) is not detected on the diffractograms. Nevertheless, the low Ag content in the solids can be responsible for this lack of detection.

Crystallite sizes of the ZnAl₂O₄ phase in the Ag/Zn_x-Al₂O₃ materials (with $x > 0.10$) were calculated using the Scherrer equation applied to the (*hkl*) reflection positioned at 2θ = 36.83°, which presents the maximum intensity within the spinel structure. Zn_{0.1}-Al₂O₃ sample has been removed due to the strong contribution of the alumina phase on the XRD signal. Fig. 1(B) displays the relationship between the calculated ZnAl₂O₄ mean crystallite size and the specific surface area of the catalysts (Table 1). As can be expected, the surface area developed decreases when the crystallite size increases. In addition, the increase in calcination temperature results in an increase of the crystal size from 5.7 nm (when Ag/Zn_{0.33}-Al₂O₃ is calcined at 600 °C) to 13.6 nm (when calcined at 1000 °C). Crystallite sizes were also checked using the Rietveld

refinement of XRD patterns, and the results are very similar to those obtained using the Scherrer equation.

3.1.3. Silver nanoparticles structure and morphology

3.1.3.1. Silver reducibility. Silver reducibility was studied by temperature-programmed reduction (TPR) analysis. Table 2 reports the temperature of the H₂ maximum consumption for the different studied catalysts (profiles not shown). It appears that silver supported catalysts show a broad H₂ consumption peak, with a maximum spread from 175 °C to 350 °C depending on the sample.

Since no significant reduction of alumina or zinc aluminate spinel is expected, this peak is assignable to the reduction of oxidized silver species (Ag⁺, Ag_n^{δ+} and Ag₂O) to metallic ones. Bethke and Kung [59] showed that this reduction peak shifts to lower temperature when the average silver particles size increases. Then, this parameter can be used to evaluate the relative silver particles size distribution. The evolution of the reduction peak temperature indicates that the average silver particles size increases with the Zn loading, as well as the calcination temperature for the Zn_{0.33}-Al₂O₃ supported samples. The temperature of the silver reduction peak observed for each catalyst is then reported versus their specific area in Fig. 2. Based on the work of Bethke and Kung [59], the remarkable correlation observed between the specific surface area and the reduction temperature indicates that the average silver particles size depends on zinc loading. So, the average silver particles size increases as well with the atomic percentage of zinc introduces in the alumina structure, and then with the calcination temperature of the support. The higher the Zn loading, the lower the silver temperature reduction, and so the higher the silver particles size.

Finally, the hydrogen consumption for each catalyst during the TPR experiments was calculated by integrating the TPR profile curves. Results enable to calculate the ratio of oxidized/metallic silver species for each material, as reported in Table 3, assuming Ag^I is reduced using the following Eqs. (4) and (5):



Table 2

Silver particles relative number and size over the catalysts, resulting of TPR characterizations.

	<i>T</i> _{red} (°C)	H ₂ consumption (μmol g ⁻¹)	Metallic silver content (%)
Ag/Al ₂ O ₃	319	31.5	66
Ag/Zn _{0.1} -Al ₂ O ₃	280	29.7	68
Ag/Zn _{0.2} -Al ₂ O ₃	264	29.7	68
Ag/Zn _{0.33} -Al ₂ O ₃	249	29.7	68
Ag/Zn _{0.33} -Al ₂ O ₃ C800	235	21.3	77
Ag/Zn _{0.33} -Al ₂ O ₃ C1000	188	18.5	80

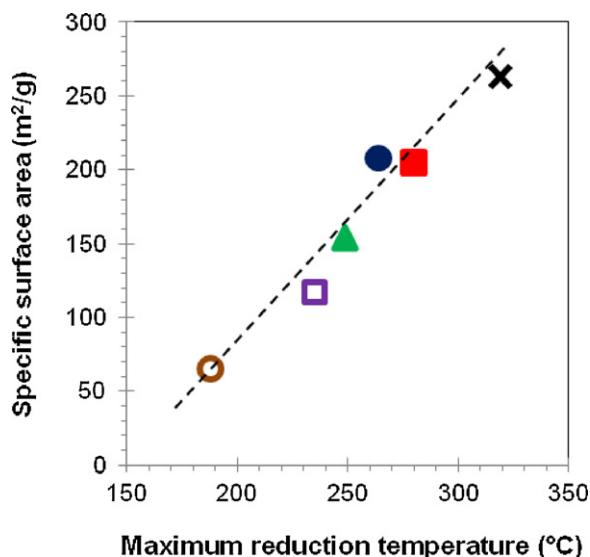


Fig. 2. Maximum reduction temperature of the catalysts observed by TPR (silver species), versus their respective surface area. (x) Ag/Al₂O₃; (■) Ag/Zn_{0.1}-Al₂O₃; (●) Ag/Zn_{0.2}-Al₂O₃; (▲) Ag/Zn_{0.33}-Al₂O₃; (□) Ag/Zn_{0.33}-Al₂O₃ C800; (○) Ag/Zn_{0.33}-Al₂O₃ C1000.



Luo et al. [28] studied the reduction of silver over alumina by TPR, and concluded that Ag⁰ content was directly proportional to the weight of impregnated silver. In the present work, two thirds of the deposited silver is in metallic state on the alumina support, after the oxidation treatment performed before the TRP test. These results are consistent with the previous work of Musi et al. [60]. Loading Zn in the alumina structure does not influence this ratio. However, increasing the calcination temperature of the Zn_{0.33}-Al₂O₃ support enhanced the part of metallic silver content, up to 80% when the support is calcined at 1000 °C.

To conclude, loading zinc in the alumina structure raises the average size of the impregnated silver particles, which are reducible at lower temperature. It does not change the ratio oxidized/metallic silver phase, contrary to raising the calcination temperature of the support to 800 °C or 1000 °C. In the next part of this work, metallic silver particles were characterized by TEM experiments, whereas UV–vis analysis provided information on the nature of the particles.

3.1.3.2. Silver morphology. The evolution of the silver nanoparticle morphology and size with the Zn²⁺ content is presented in Fig. 3. Firstly, it is noteworthy that silver particles observed by TEM over the catalysts surface are mostly metallic. Indeed, particles present

inter-reticular distances of $d \approx 2.3 \text{ \AA}$. Some of them show two distances, $d \approx 2.3 \text{ \AA}$ and $d \approx 2 \text{ \AA}$, with an angle of 70° between them. These parameters are characteristics of Ag⁰ in face centered cubic configuration (ICCD PDF no. 01-089-3722).

The Ag/Al₂O₃ sample presents the lower silver particles size distribution, most of the particles ranging below 10 nm. The Zn²⁺ insertion in the alumina matrix leads to an increase in the silver particle size. Starting from Zn = 10 at.%, larger silver particles are observed, even if most of the particles present size below 10 nm, as observed for the Ag/Al₂O₃ catalyst. The presence of very large particles and the formation of aggregates are however clearly observed on the Ag/Zn_{0.33}-Al₂O₃ material. These large particles are clearly observed in Fig. 3(G), and the formation of aggregates is depicted in Fig. 3(H). While the mean elementary particle size seems to increase over the Zn-doped supports, it is always possible to observe small particles, even at high Zn²⁺ content (see Fig. 3(I)).

The effect of the calcination temperature on the silver particle size and repartition in the support is clearly observed in Fig. 4. Indeed, the increase in calcination temperature from 600 °C (Fig. 3(G–I)) to 800 °C (Fig. 4(A–C)) seems to induce only a slight increase in particle size. Indeed, the formation of large particle is always observed (Fig. 4(A)), but some zone of the support seems to be enriched in silver.

The presence of small particles (below 10 nm) is however always observed (Fig. 4(B and C)). After calcination at 1000 °C, the Ag particle and aggregate sizes are however largely increased, as it can be observed on the HAADF image (Fig. 4(D)). Indeed, while the Ag particles are difficult to observe by HAADF after calcinations at 600 °C (Fig. 3(E) for Ag/Zn_{0.10}-Al₂O₃; similar images were however obtained for all materials calcined at the same temperature), the Ag particles are clearly observed after calcination at 1000 °C. In addition, direct TEM observation allows the easy detection of the large particles, or aggregates of particles (Fig. 4(E and F)). Nevertheless, some small particles (~5–10 nm) remain observable by TEM (Fig. 4(F)).

TEM analysis should be used with caution when studying silver-based catalysts due to the possible dissolution/precipitation, and formation of large particles, during sample preparation for TEM analysis. Nevertheless, the contribution of this step should be logically considered as similar for all materials. Then, TEM observation is suggesting that both zinc introduction and raising the calcination temperature result in an increase in the mean silver metallic particle size, especially when the calcination temperature reached 1000 °C. These results are consistent with the TPR study, which showed that loading zinc in the alumina structure raises the average size of the impregnated silver particles.

3.1.3.3. Silver state. UV–visible is used to evaluate the state of silver supported nanoparticles on the different supports. The corresponding UV–vis spectra are presented in Fig. 5, completed by attributions of the UV–visible bands based on the literature data. In order to focus on silver absorption bands, the support contribution spectrum was subtracted for each catalyst. Fig. 5(A) shows the influence of the zinc loading inside the alumina structure, whereas Fig. 5(B) highlights the calcination temperature impact on Ag/Zn_{0.33}-Al₂O₃ properties.

It is largely reported in the literature that UV–vis spectra cannot provide quantitative data of silver state on alumina, essentially due to (i) the high extinction coefficients for Ag_n^{δ+} and Ag_n⁰ clusters compared to that of Ag⁺ ions and (ii) to the fact that some types of Ag⁺ ions are not detectable. However, the deconvolution into Gaussian subbands of UV–vis spectra can be performed to obtain, by integrated the peak area, an underestimate percentage of Ag⁺ ions compared to Ag_n^{δ+} and Ag_n⁰ clusters. Results are reported in Fig. 6 and enable to assess the distribution of the detectable silver

Table 3

Effect of zinc addition over the ethanol and NO_x conversion at 300 °C and 450 °C. Comparison between the supports and the corresponding silver supported catalysts.

Catalysts	Conv. EtOH (%)		Conv. NO _x (%)	
	300 °C	450 °C	300 °C	450 °C
Al ₂ O ₃	30	100	2	21
Ag/Al ₂ O ₃	95	100	74	100
Zn _{0.1} -Al ₂ O ₃	27	100	1	10
Ag/Zn _{0.1} -Al ₂ O ₃	76	100	51	98
Zn _{0.2} -Al ₂ O ₃	26	100	0	22
Ag/Zn _{0.2} -Al ₂ O ₃	99	100	86	99
Zn _{0.33} -Al ₂ O ₃	25	100	2	16
Ag/Zn _{0.33} -Al ₂ O ₃	100	100	87	100
Zn _{0.33} -Al ₂ O ₃ C800	28	100	2	22
Ag/Zn _{0.33} -Al ₂ O ₃ C800	100	100	100	100
Zn _{0.33} -Al ₂ O ₃ C1000	17	100	2	24
Ag/Zn _{0.33} -Al ₂ O ₃ C1000	65	100	7	56

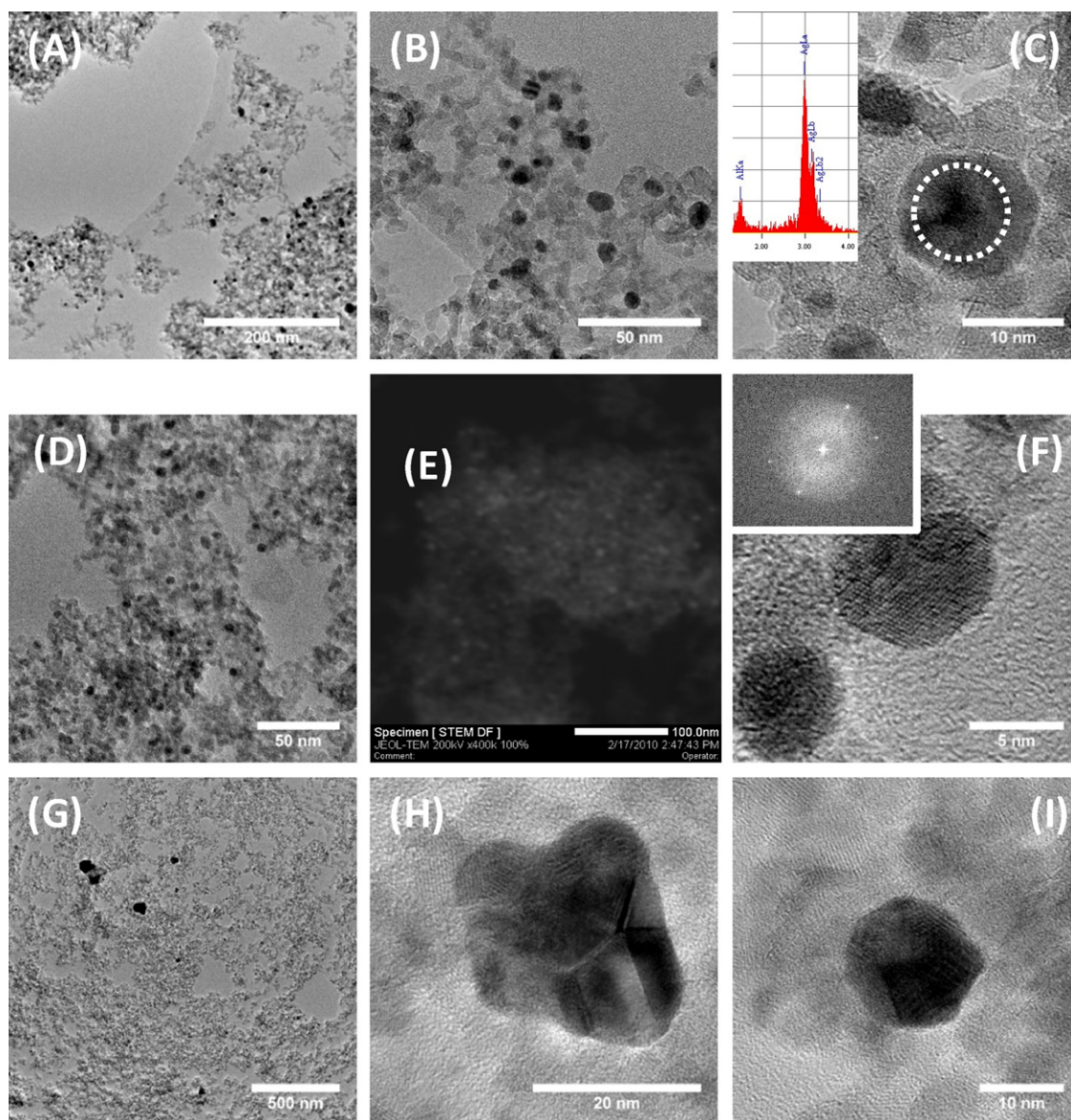


Fig. 3. Representative TEM images obtained for (A–C) Ag/Al₂O₃ [inset: EDX spectrum recorded on the defined zone in (c)]; (D–F) Ag/Zn_{0.10}-Al₂O₃ [(E) is the HAADF image; (F) inset is the FFT of the 5 nm particle]; (G–I) TEM images at different magnifications for Ag/Zn_{0.33}-Al₂O₃. All samples were calcined at 600 °C.

species on the whole materials. In fact, peaks at about 200–230 nm and 250–260 nm are assigned to highly dispersed silver ions (Ag⁺) and oxidized silver clusters (Ag_n^{δ+}), respectively. Bands located at 290 nm and 350 nm are attributed to metallic silver cluster (Ag_n⁰). An approximation of the silver state distribution over the catalysts is then obtained. Fig. 6 presents the contribution of each silver species detected by UV–visible, versus the percentage of zinc added into the alumina network (Fig. 6(A)), and the calcination temperature of Zn_{0.33}-Al₂O₃ (Fig. 6(B)).

Results shows that zinc loading into the alumina network strongly impacts the silver state of the catalysts. In fact, Fig. 6(A) shows that Zn incorporation ($x=0.1\%$, 0.2% and 0.3%) leads to decrease by more than half the contribution of the Ag⁺ ions band ($\lambda < 250$ nm). In parallel, increases of the contribution of oxidized Ag_n^{δ+} cluster (band at $\lambda = 250$ –260 nm) and Ag_n⁰ metallic (band at ~ 300 nm) are observed. A slight increase of the metallic Ag_n⁰ clusters with $n \geq 8$ ($\lambda = 350$ nm) is observed when $x=0.1\%$ and 0.2% . These results suggest that the addition of zinc into the alumina structure favored the sintering of the dispersed Ag⁺ ions, obtained

at the end of the silver impregnation step, into silver oxidized (Ag_n^{δ+}) clusters and metallic (Ag⁰) species.

Fig. 6(B) shows that the increase in calcination temperature (case of Ag/Zn_{0.33}-Al₂O₃) to 800 °C and then 1000 °C leads to a diminution of the amount of Ag_n^{δ+} clusters ($\lambda = 250$ –260 nm) and metallic Ag⁰ (band at ~ 300 nm), while highly dispersed silver ions (Ag⁺, $\lambda < 250$ nm) are enhanced compared to catalysts calcined at 600 °C. Increasing the calcination temperature up to 1000 °C enables the observation of the surface plasmon resonance (SPR) phenomenon, linked to nanoparticles or aggregates of metallic silver Ag⁰ larger than 10 nm ($\lambda > 390$ nm) [35,57,63]. It is noteworthy that these metallic particles, responsible for the SPR phenomenon, do not contribute to the metallic Ag⁰ band at around 300 nm. Compared with TEM results, it is likely that this band (λ around 300 nm) is characteristic of Ag⁰ particles larger than 100 nm, which are not observed with Ag/Zn_{0.33}-Al₂O₃ C1000, contrary to Ag/Zn_x-Al₂O₃ ($x=0.1$; 0.2 ; 0.33) and Ag/Zn_{0.33}-Al₂O₃ C800. It implies that SPR phenomenon is rather linked to silver nanoparticles in the 10–100 nm range.

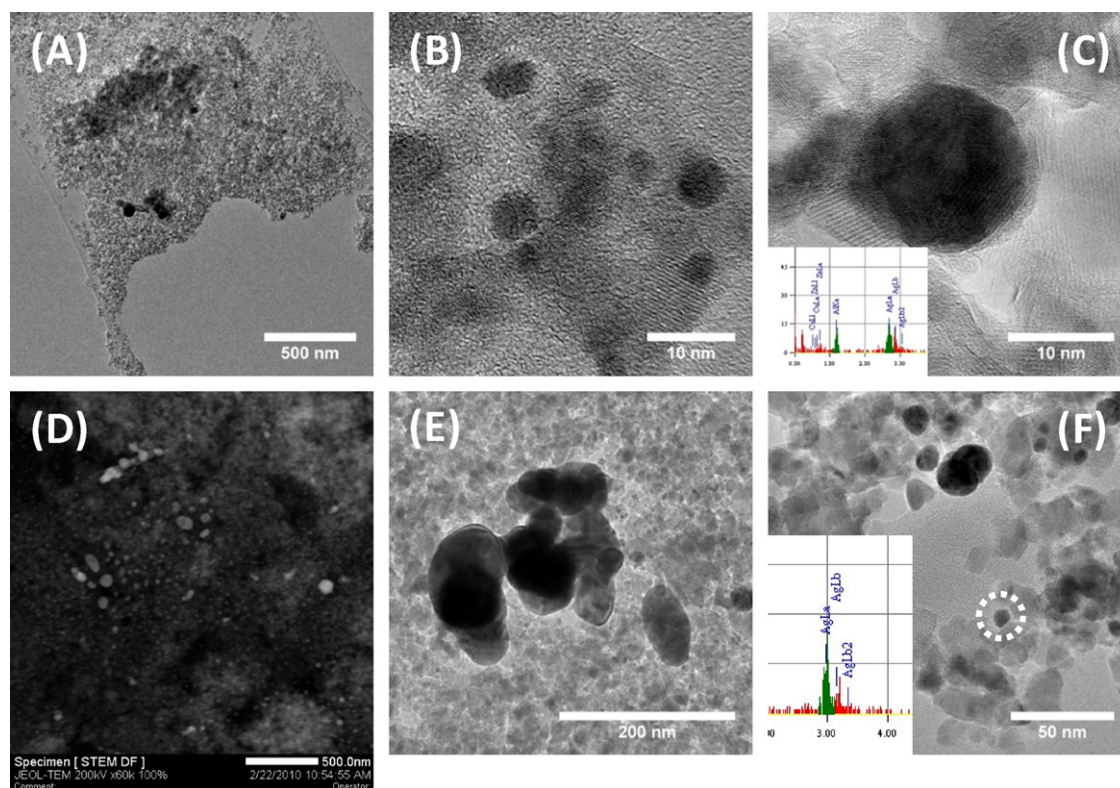


Fig. 4. Representative TEM images obtained for $\text{Ag/Zn}_{0.33}\text{-Al}_2\text{O}_3$ after calcination at 800°C (A–C) and 1000°C (D–F).

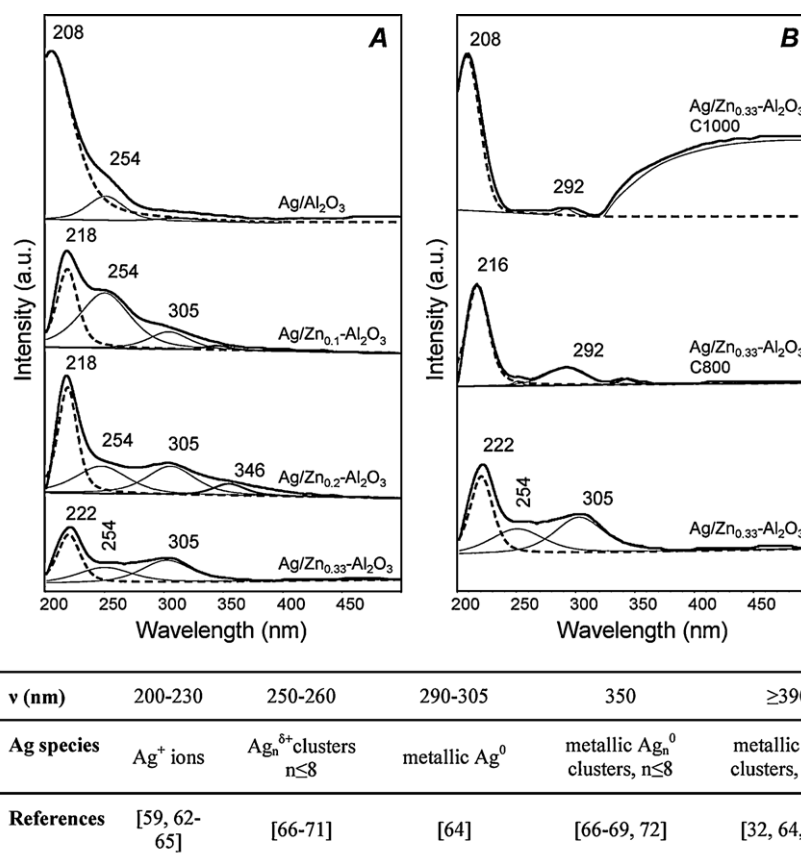


Fig. 5. Ex situ UV–visible spectra and deconvolution of the silver supported catalysts. (A) Influence of the zinc loading; (B) influence of the calcination temperature.

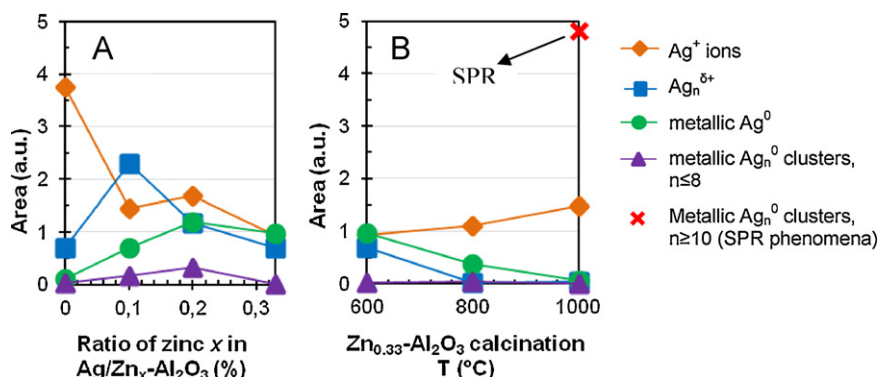


Fig. 6. Deconvoluted area of silver species obtained in UV-visible. (A) Influence of zinc addition; (B) influence of the calcination temperature. (♦) Ag⁺ ions; (■) Ag_n^{δ+}; (●) metallic Ag⁰; (▲) metallic Ag_n⁰ clusters, $n \leq 8$; (×) metallic Ag_n⁰ clusters, $n \geq 10$ (SPR phenomena).

Finally, these spectra confirm that all samples contain oxidized silver species (Ag⁺, Ag_n^{δ+}) and metallic silver species (Ag_n, Ag⁰), with repartition depending on the support. Zinc incorporation to the alumina-based network leads to enhance the contribution of oxidized Ag_n^{δ+} clusters, but also metallic silver. Nevertheless, no important modification of silver state is denoted in regards of Zn loading (i.e. 10%, 20% or 33%). In parallel, increasing the calcination temperature of the support from 600 °C to 800 °C then 1000 °C enables to maintain the amount of silver cationic species (Ag⁺).

3.2. Acid–base surface properties

In this part, the effects of zinc addition over the surface properties of the catalysts are studied. Acid–base properties, as well as residual OH groups of alumina-based supports, were investigated using pyridine and CO₂ adsorption monitored by IR spectroscopy.

The CO₂ adsorption experiments show similar carbonate species in nature and in number on each material, denoting that zinc addition has little influence on the basic characters of the host alumina (spectra not shown).

Fig. 7 compares the IR spectra in the OH stretching region of the Ag catalysts supported over pure alumina and Zn doped alumina

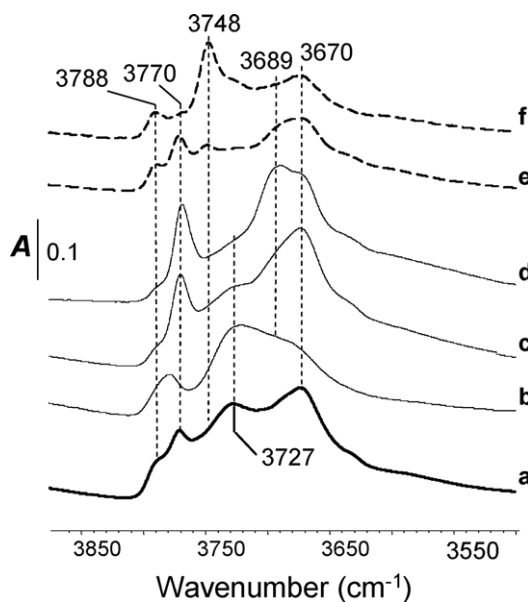


Fig. 7. IR spectra in the ν_{OH} region of alumina and zinc-doped alumina catalysts, activated at 450 °C. (a) Ag/Al₂O₃; (b) Ag/Zn_{0.1}-Al₂O₃; (c) Ag/Zn_{0.2}-Al₂O₃; (d) Ag/Zn_{0.33}-Al₂O₃; (e) Ag/Zn_{0.33}-Al₂O₃ C800; (f) Ag/Zn_{0.33}-Al₂O₃ C1000.

supports, after outgassing at 450 °C. The IR spectrum of the reference Al₂O₃ catalyst is consistent with that previously reported in the literature [72]. Results show different types of OH groups on alumina, displaying bands at 3788, 3770, 3727 and 3670 cm⁻¹. The spectra of Zn doped samples are significantly different for the free OH groups.

The band at 3770 cm⁻¹ on Ag/Al₂O₃ catalyst is assigned to the Type Ia of the Tsyganenko model [73,74]. This type is attributed to OH groups coordinated to one Al³⁺ in tetrahedral coordination, at the surface layers of alumina. These OH groups are the most affected by the addition of zinc in the alumina structure: the higher the Zn loading, the higher the intensity of the band at 3770 cm⁻¹. In contrast, this band decreases when the calcination temperature of Ag/Zn_{0.33}Al₂O₃ is raised to 800 °C then 1000 °C (dotted lines in Fig. 7).

IR spectra of catalysts loaded with 20% and 33% of zinc, along with Ag/Zn_{0.33}Al₂O₃ C800, display a new band detected at 3689 cm⁻¹. Ag/Zn_{0.22}Al₂O₃ C800 and Ag/Zn_{0.33}-Al₂O₃ C1000 catalysts also exhibit another band at 3748 cm⁻¹, particularly intensive for the latest catalyst. It is noteworthy that Ag/Zn_{0.33}-Al₂O₃ C1000 spectrum has similarities with other alumina spinel structure based on zinc [75], magnesium [76] or cobalt [77]. Finally, Type III acidic OH groups (ν_{OH} at 3670 cm⁻¹) are not significantly affected by the zinc addition.

In conclusion, the differences in the features of the catalysts IR spectra can be related to their modifications with Zn. Indeed, γ -Al₂O₃ and Zn_x-Al₂O₃ ($x = 0.1; 0.2; 0.33$) materials present a spinel-type structure. But zinc aluminate samples have rather a normal structure [78] whereas alumina is a defective spinel. Based on these results, it seems that the spinel structure is formed starting from 10 at.% Zn loading, in accordance with the XRD analysis.

The surface acidity was determined by IR spectroscopy of adsorbed pyridine, which is one of the most largely used basic probe molecules for surface acidity characterization [79]. Due to the nitrogen electron lone pair, pyridine interacts with acidic centers in a specific way to form (i) the pyridinium ion on protonic sites (PyH⁺) and (ii) coordinated species on Lewis acid sites (PyL), giving rise to ν_{8a} , ν_{8b} , ν_{19a} and ν_{19b} ring vibration modes. Pyridine (200 Pa at equilibrium) was adsorbed at room temperature, and then desorbed by temperature steps of 50 °C up to 450 °C.

Fig. 8 presents the IR spectra of the catalysts when pyridine is evacuated at 200 °C. In such conditions, only pyridine coordinated on LAS is observed. No IR bands assigned to pyridinium ion were detected, as expected on alumina, which does not exhibit OH groups strong enough to protonate the pyridine. Characteristic IR absorption bands are displayed at 1623, 1617, 1575, 1495 and 1452 cm⁻¹ on the reference Al₂O₃ support (Fig. 8, spectrum (a)), as well as on Zn doped materials (spectra (b)–(f)).

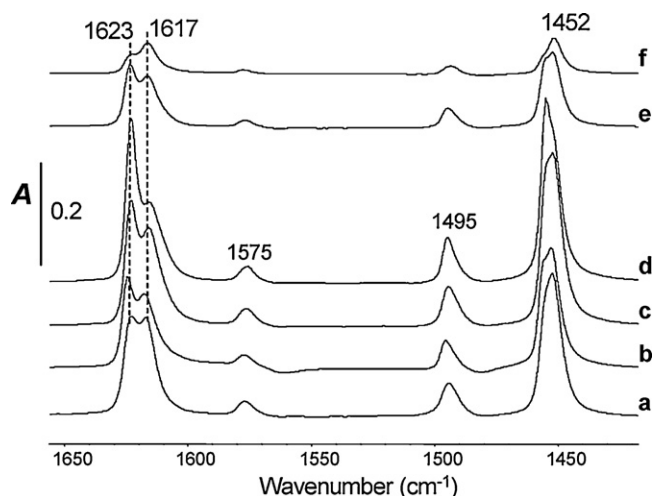


Fig. 8. IR difference spectra of pyridine desorbed at 200 °C. (a) Ag/Al₂O₃; (b) Ag/Zn_{0.1}-Al₂O₃; (c) Ag/Zn_{0.2}-Al₂O₃; (d) Ag/Zn_{0.33}-Al₂O₃; (e) Ag/Zn_{0.33}-Al₂O₃ C800; (f) Ag/Zn_{0.33}-Al₂O₃ C1000.

In order to study the influence of zinc incorporation over LAS, two adsorption modes can be assessed. The first one (ν_{8a}) enables the description of the LAS strength, whereas the second one (ν_{19b}) allows the quantification of the total amount of coordinated pyridine, obtained from the surface area of its absorption band using its molar coefficient ($\epsilon_{\nu_{19b}} = 1.5 \text{ cm}^2 \mu\text{mol}^{-1}$ [52,58]). In the ν_{8a} range, two bands can be distinguished on the reference alumina (Fig. 7, spectrum a) at 1623 cm⁻¹ and 1617 cm⁻¹, assigned to pyridine coordinated to tetrahedral Al³⁺ (strong LAS) and to both tetrahedral and octahedral Al³⁺ (medium to weak LAS), respectively. Influence of the zinc addition in the alumina structure over the LAS strength was assessed using the area of ν_{19b} band (total LAS), whereas the ν_{8a} deconvolution enables to obtain the distribution, in $\mu\text{mol g}^{-1}$, of pyridine coordinated to strong and medium LAS, as explained in the experimental part. Total and strong LAS amount was reported in function of pyridine temperature evacuation in Fig. 9(A) and (B) respectively. It appears that total LAS concentration is not strongly affected by Zn loading. To the opposite, rising the calcination temperature of the support (Ag/Zn_{0.33}-Al₂O₃ C800 and Ag/Zn_{0.33}-Al₂O₃ C1000 materials) decreases the total amount of LAS. Concerning the distribution of coordinative unsaturated sites (Fig. 9(B)), both the Zn incorporation in the alumina network and the temperature calcination strongly impact the concentration of strong LAS. In fact, it appears that the higher the

Zn loading, the higher the strong LAS amount. Raising the calcination temperature from 600 °C to 800 °C and 1000 °C leads to decrease the concentration of strong LAS. It is worth noting that the Ag/Zn_{0.33}-Al₂O₃ C800 catalyst presents homogeneous strong LAS population. To conclude, doping the alumina host support by Zn leads to modify the Al_{IV}³⁺/Al_{VI}³⁺ coordinative unsaturated sites ratio.

3.3. NO_x selective catalytic reduction with ethanol

3.3.1. NO_x and ethanol conversion

In this part, the catalytic tests of the NO_x selective catalytic reduction with ethanol (EtOH-SCR) are presented. Influence of silver addition over the alumina support is discussed, as well as the influence of zinc addition.

Fig. 10 shows that silver addition over the alumina support leads to enhance both the NO_x and ethanol conversions, as reported by Miyadera [27]. The effect of silver addition is more striking concerning NO_x conversion which is total in the 350–450 °C temperature range over Ag/Al₂O₃. Effect of zinc addition over these parameters is presented in Table 3 at 300 °C and 450 °C, which are representatives of the materials activity. At 300 °C, results showed that addition of 10 at.% of zinc in the alumina structure decreases the ethanol conversion, from 95% to 76%, as well as the NO_x conversion from 74% to 51%. However, addition of 20 and 33 at.% of zinc leads to better results in NO_x and ethanol conversions than with the Ag/Al₂O₃ reference catalyst. Then, raising the calcination temperature of Zn_{0.33}-Al₂O₃ to 800 °C leads to even better results in NO_x conversion, which reaches 100% at 300 °C. However, raising more the calcination temperature of the support to 1000 °C leads to inhibit the activity, even compared to Ag/Al₂O₃. For instance, NO_x conversion reaches only 7% at 300 °C, contrasting with the total conversion obtained when Ag/Zn_{0.33}-Al₂O₃ is calcined at 800 °C.

At 450 °C, the ethanol conversion is total (or almost) for all the supports and catalysts. No major differences are observed concerning NO_x conversion, excepted for Ag/Zn_{0.33}-Al₂O₃ C1000 which shows very low activity compared to the other catalysts. Indeed, its NO_x conversion reaches only 56%.

3.3.2. Selectivity in N-products

In this part, the distribution of the nitrogen containing products observed during the EtOH-SCR test is discussed. First, it is worth mentioning that N₂O emissions have not been observed over the different supports, or silver supported samples. Firstly, the influence of the silver addition over pure alumina is presented.

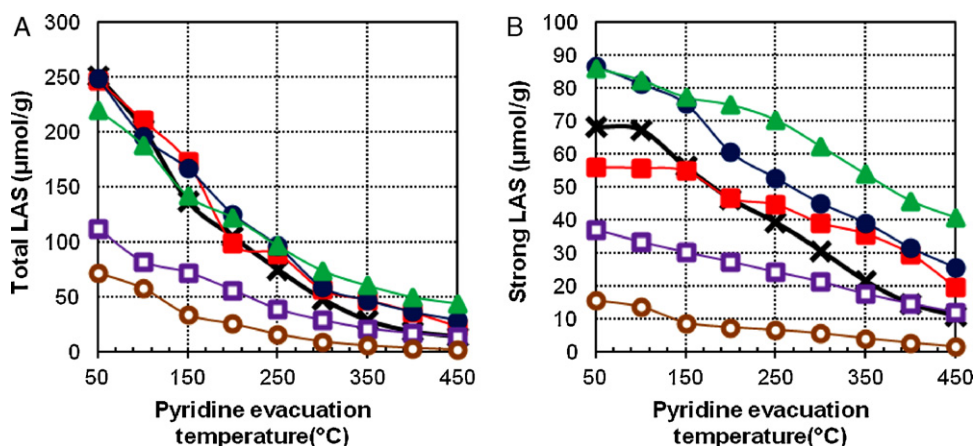


Fig. 9. Evolution of the concentration ($\mu\text{mol g}^{-1}$) of the total LAS and strong LAS versus the pyridine evacuation temperature. (×) Ag/Al₂O₃; (■) Ag/Zn_{0.1}-Al₂O₃; (●) Ag/Zn_{0.2}-Al₂O₃; (▲) Ag/Zn_{0.33}-Al₂O₃; (□) Ag/Zn_{0.33}-Al₂O₃ C800; (○) Ag/Zn_{0.33}-Al₂O₃ C1000.

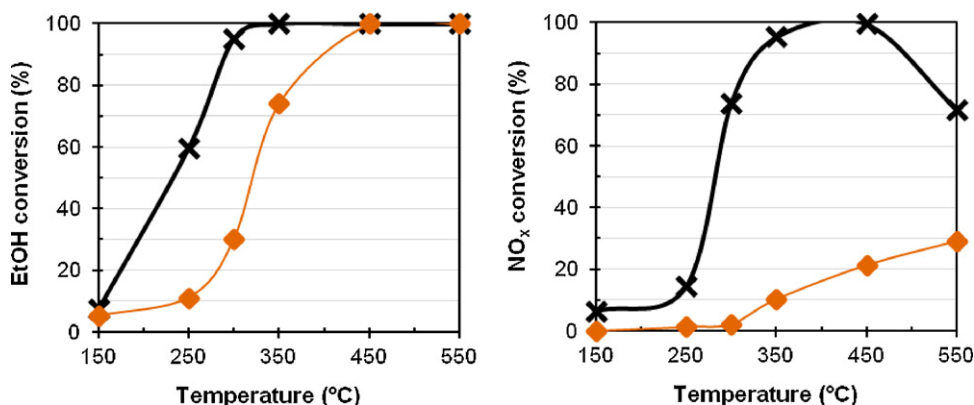


Fig. 10. Effect of silver addition over ethanol and NO_x conversion in EtOH-SCR tests. (♦) Al₂O₃; (×) Ag/Al₂O₃.

Fig. 11 shows that NO is strictly converted into NO₂ and N₂ over alumina, in the same proportion at 350 °C and 450 °C. NO oxidation is however favored at 550 °C.

Concerning the NO conversion over Ag/Al₂O₃ catalyst (Fig. 11(B)), two behaviors are observed depending on the temperature range. Precisely, at low temperature ($T \leq 350$ °C), only NO₂ and N₂ are emitted, whereas at higher temperature, NO is mainly converted into N₂ and NH₃, with a maximum ammonia yield of 27% at 450 °C. Finally, compared to the supports alone, the distribution of the N-products strongly differs. The impact of the support composition over the NO_x conversion into nitrogen is depicted for each silver supported catalyst in Fig. 12.

Fig. 12(A) shows that addition of 10 at.% zinc in the alumina structure decreases the nitrogen yield in the 250–550 °C temperature range, according with the decrease of the NO_x conversion depicted in the previous section. However, addition of 20 and 33 at.% zinc increases the N₂ yield from 74% to 86–87% at 300 °C. At 350 °C, only the addition of 20 at.% of zinc leads to a better result compared to the Ag/Al₂O₃ reference catalyst, with an increase of the nitrogen yield from 87 to 96%.

Then, Fig. 12(B) shows that raising the calcination temperature of Zn_{0.33}-Al₂O₃ from 600 °C to 800 °C leads to an enhancement of the N₂ yield over almost the whole temperature range. Compared to Ag/Al₂O₃, the N₂ formation is satisfactorily improved at 250 °C (from 14% to 25%) and at 300 °C (from 74% to 100%). Raising the calcination temperature of Zn_{0.33}-Al₂O₃ to 1000 °C leads to a major decrease of the activity. Indeed, nitrogen yield solely reaches 7% at 300 °C.

Finally, these results clearly show that zinc loading can be a sustainable solution to enhance the activity of Ag/Al₂O₃ in EtOH-SCR at low temperature, which seems easier in a practical way than adding another reductant like H₂ [53] in the gas mixture.

Table 4

Effect of zinc addition over the NH₃ and NO₂ emission at 250 °C and 450 °C. Comparison between the supports and the corresponding silver supported catalysts.

Catalysts	NH ₃ yield (%)		NO ₂ yield (%)	
	250 °C	450 °C	250 °C	450 °C
Al ₂ O ₃	0	0	0	22
Ag/Al ₂ O ₃	0	27	36	0
Zn _{0.1} -Al ₂ O ₃	0	0	0	2
Ag/Zn _{0.1} -Al ₂ O ₃	0	31	12	0
Zn _{0.2} -Al ₂ O ₃	0	0	0	11
Ag/Zn _{0.2} -Al ₂ O ₃	0	30	7	0
Zn _{0.33} -Al ₂ O ₃	0	0	0	10
Ag/Zn _{0.33} -Al ₂ O ₃	0	52	5	0
Zn _{0.33} -Al ₂ O ₃ C800	0	0	0	7
Ag/Zn _{0.33} -Al ₂ O ₃ C800	0	33	9	0
Zn _{0.33} -Al ₂ O ₃ C1000	0	0	0	1
Ag/Zn _{0.33} -Al ₂ O ₃ C1000	0	0	2	0

However, it requires a control of both the Zn loading inside the alumina structure, and the calcination temperature of the material.

Concerning the reaction selectivity, the NH₃ and NO₂ yields at 250 °C and 450 °C are reported in Table 4 for each support and silver supported catalyst. These temperatures are therefore representatives of the catalysts selectivity at low and higher temperature.

The differences in N-products distribution (pointed out previously in Fig. 11) between the support and the corresponding silver supported catalyst are here highlighted.

Indeed, at 250 °C, neither NO₂ nor NH₃ emissions are observed over the supports. However, addition of silver leads to the oxidation of NO in NO₂ at this temperature for every catalyst. Still, no ammonia emission is observed.

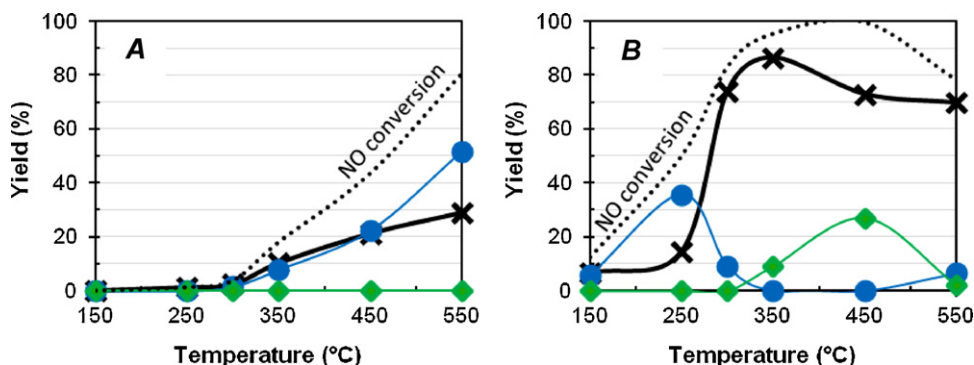


Fig. 11. Yield of nitrogen products observed during EtOH-SCR tests. (×) N₂; (•) NO₂; (♦) NH₃. (A) Al₂O₃ and (B) Ag/Al₂O₃.

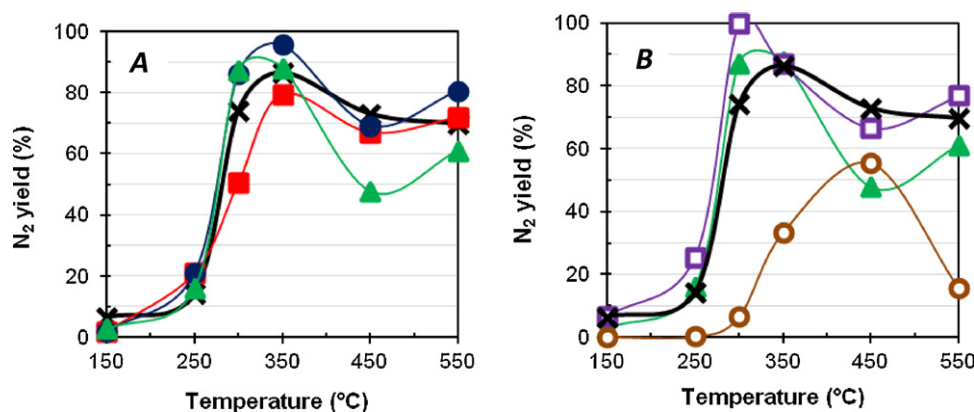


Fig. 12. Influence of (A) the zinc loading inside Al₂O₃ structure and (B) the calcination temperature of Zn_{0.33}-Al₂O₃ over the nitrogen yield in EtOH-SCR tests. (×) Ag/Al₂O₃; (■) Ag/Zn_{0.1}-Al₂O₃; (●) Ag/Zn_{0.2}-Al₂O₃; (▲) Ag/Zn_{0.33}-Al₂O₃; (□) Ag/Zn_{0.33}-Al₂O₃ C800; (○) Ag/Zn_{0.33}-Al₂O₃ C1000.

At 450 °C, if NO₂ emission is observed for every support, addition of silver leads to a disappearance of this emission. On the other hand, emission of ammonia is then observed. Compared with Table 3 and Fig. 12, it appears that, at 450 °C and for the whole silver supported catalysts, NO_x are strictly converted into NH₃ and N₂.

These results clearly show that addition of silver drastically transformed the NO_x chemistry observed over the supports alone. The role of the silver sites in the EtOH-SCR process will be developed in the discussion section. The following part presents the transformation of ethanol in carbonated products.

3.3.3. Carbonated products

In this part, the carbonated products emitted during the EtOH-SCR tests with Al₂O₃ and Ag/Al₂O₃ are firstly presented. Then, the influence of the zinc addition over these emissions is developed.

On the alumina support alone, ethanol is converted into CO₂, ethylene, acetaldehyde and CO (Fig. 13). However, ethanol is principally converted into ethylene, especially above 300 °C. The C₂H₄ yield reaches 73% at 450 °C.

Addition of silver leads to different results. Indeed, ethanol is then mainly converted into CO₂. Emission of acetaldehyde is observed between 150 °C and 350 °C, with a maximum yield of 28% at 250 °C, which shows that Ag favored its formation at low temperature, compared to the support alone. Besides, ethylene emission is suppressed. It suggests that silver interferes with the active sites of the support, responsible for the transformation of ethanol in ethylene. A second assumption is that ethylene is consumed during SCR reaction, as a primary product of C₂H₅OH reduction. This point will be discussed in the following part. Finally, emission of CO is also observed, mainly for the higher temperatures.

This study shows that ethanol can be converted into numerous carbonated by-products during the EtOH-SCR process. Alumina and silver species sites are responsible for their formation, depending on the temperature range. Acetaldehyde, ethylene or CO products can thereafter react with NO to perform the SCR reaction. The reactivity of each of these by-products in NO SCR with Ag/Al₂O₃ has been evaluated, keeping the same carbon concentration, at 2400 ppm. Firstly, CO is not able to perform SCR in this condition, and ethylene is active only at 550 °C (results not shown), which is a too high temperature to consider ethylene as the main reducing agent for NO_x abatement. In opposite, results obtained with acetaldehyde as reducer (Table 5) show that the CH₃CHO-SCR activity is very low at 250 °C, but gradually increases with temperature to be very consistent at 350 °C.

Table 5

Acetaldehyde conversion and nitrogen yield obtained on Ag/Al₂O₃ catalyst. 1200 ppm CH₃CHO, 400 ppm NO, 500 ppm CO, 167 ppm H₂, 8% O₂, 10% H₂O and 10% CO₂ balanced in nitrogen. GHSV = 150,000 h⁻¹.

	Temperature		
	250 °C	300 °C	350 °C
Conv. CH ₃ CHO	4%	38%	73%
N ₂ yield	4%	20%	84%

Based on these results, Table 6 reports the emission of acetaldehyde obtained during the EtOH-SCR experiments at 250 °C and 350 °C for the supports and the silver supported catalysts.

Concerning the Zn_x-Al₂O₃ supports, same results as those presented on Al₂O₃ are obtained, showing that addition of zinc does not significantly increase the acetaldehyde emission at 250 °C or 350 °C, compared with pure alumina. Concerning the silver supported catalysts, Table 6 shows that CH₃CHO emission grows compare to the silver free supports. At 250 °C, the higher acetaldehyde yield is observed for the Ag/Zn_{0.33}-Al₂O₃ C800 catalysts, whereas the lower one is observed with Ag/Zn_{0.1}-Al₂O₃ and Ag/Zn_{0.33}-Al₂O₃ C1000 materials. At 350 °C, addition of zinc leads to an increase of the acetaldehyde emission of silver supported catalysts, except for Ag/Zn_{0.33}-Al₂O₃ C800 which presents no CH₃CHO emission. These differences will be further developed in Section 4 below.

Table 6

EtOH-SCR: effect of zinc addition over the acetaldehyde emission at 250 °C and 350 °C. Comparison between the supports and the corresponding silver supported catalysts.

Catalysts	CH ₃ CHO yield (%)	
	250 °C	350 °C
Al ₂ O ₃	2	11
Ag/Al ₂ O ₃	27	2
Zn _{0.1} -Al ₂ O ₃	2	14
Ag/Zn _{0.1} -Al ₂ O ₃	15	16
Zn _{0.2} -Al ₂ O ₃	1	5
Ag/Zn _{0.2} -Al ₂ O ₃	30	12
Zn _{0.33} -Al ₂ O ₃	1	5
Ag/Zn _{0.33} -Al ₂ O ₃	29	10
Zn _{0.33} -Al ₂ O ₃ C800	1	7
Ag/Zn _{0.33} -Al ₂ O ₃ C800	47	0
Zn _{0.33} -Al ₂ O ₃ C1000	3	15
Ag/Zn _{0.33} -Al ₂ O ₃ C1000	18	35

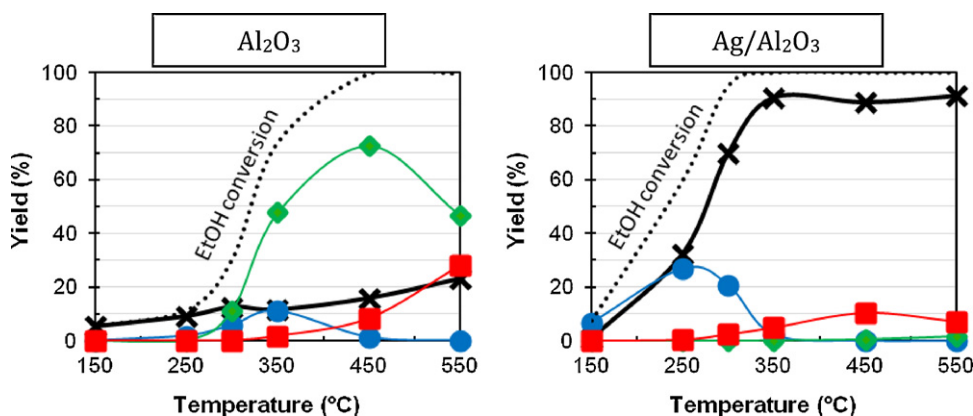


Fig. 13. Yield of carbonated products observed with Al_2O_3 and $\text{Ag}/\text{Al}_2\text{O}_3$ during EtOH-SCR tests. (x) CO_2 ; (●) acetaldehyde; (◆) ethylene; (■) CO.

4. Discussion

Silver supported catalysts on alumina-based oxides show that incorporation of Zn into Al_2O_3 strongly influences (i) the structural and chemical surface properties of the support and (ii) the silver state. XRD results indicate the formation of zinc aluminate spinel structure, leading to a modification of the $\text{Al}_{\text{IV}}^{3+}/\text{Al}_{\text{VI}}^{3+}$ coordinative unsaturated sites ratio. From UV-vis results, it appears that silver is mainly present as highly dispersed silver ions (Ag^+) on $\text{Ag}/\text{Al}_2\text{O}_3$ samples. Zn addition enhances the amount of oxidized $\text{Ag}_n^{\delta+}$ cluster and metallic Ag^0 species but drop down the percentage of Ag^+ . Besides, TEM and TPR experiments indicate that the higher the Zn loading, the higher the silver metallic particle size. Catalytic results show that the reduction of NO_x by ethanol starts at 250 °C, and gradually increases to 100% at $T \geq 350$ °C (Fig. 10). Based on these results, two range of temperature were studied separately ($T \leq 350$ °C and $T \geq 350$ °C) in the following section.

4.1. Nitrogen formation at low temperature ($T \leq 350$ °C)

At low temperature (i.e. $T \leq 350$ °C) EtOH-SCR test (Fig. 13 and Table 6) shows that CH_3CHO is one of the main carbonated compounds detected at 250 °C, when the NO_x conversion is low. Indeed, acetaldehyde yield reaches 47% at 250 °C for the $\text{Ag}/\text{Zn}_{0.33}\text{-Al}_2\text{O}_3$ C800 catalyst, whereas 25% of NO_x are converted. As reported in the literature [37,80], the acetaldehyde reactivity is the first step in EtOH-CR mechanism. Thus, the NO_x reduction with CH_3CHO (CH_3CHO -SCR) was studied over the whole samples. Results reported in Table 5 show that acetaldehyde conversion increases with temperature, from 4% to 73%, at 250 °C and 350 °C respectively. In parallel, N_2 yield grows from 4% to 84%. From these results, it appears that acetaldehyde is not an effective NO_x reducer at 250 °C, contrary to 350 °C. As a matter of comparison, in usual EtOH-CR test, N_2 yield rates between 18% and 27% at 250 °C (Fig. 12) and CH_3CHO yield can reach 47%. Thus, CH_3CHO emitted at 250 °C from EtOH-SCR can be used to assess the dehydrogenation activity of the catalysts. In addition, CH_3CHO detected at higher temperature (i.e. 350 °C), when NO_x reduction is effective, illustrates the consumption of CH_3CHO for the NO_x reduction. So, it is proposed that the gap between the acetaldehyde yield measured at 250 °C and 350 °C (Table 6) during the EtOH-SCR test (denoted as CH_3CHO activity) is an experimental parameter representative of the catalyst activity in CH_3CHO -SCR. Based on this assumption, Fig. 14(A) reports the N_2 yield versus the CH_3CHO activity parameter. The higher the gap between acetaldehyde yield at 250 °C and 350 °C, the higher the CH_3CHO activity. Whatever the catalysts used in this work, the nitrogen yield at 300 °C increases alongside the CH_3CHO activity, showing that the higher the CH_3CHO activity

parameter, the higher the N_2 production. This result confirms that key parameters in EtOH-SCR are (i) the activation of the ethanol dehydrogenation reaction, and (ii) the acetaldehyde reactivity in DeNO_x mechanism.

Finally, $\text{Ag}/\text{Zn}_{0.33}\text{-Al}_2\text{O}_3$ C800 catalyst is the sample who presents the higher CH_3CHO activity (+50%), leading to the highest NO_x conversion into N_2 . Table 6 shows that the main difference between this catalyst and $\text{Ag}/\text{Al}_2\text{O}_3$ is the CH_3CHO formation at 250 °C, which is 20 yield points higher for $\text{Ag}/\text{Zn}_{0.33}\text{-Al}_2\text{O}_3$ C800. No significant differences are observed in CH_3CHO consumption at 350 °C. Yet, it is well known that ethanol dehydrogenation occurs either on the support basic sites or on the metal function of the catalyst [81]. However, since no differences in basic sites have been observed over the different samples, it is likely that the silver phase is responsible for the variation in the acetaldehyde formation at 250 °C.

In this work, silver characterizations were performed using TEM, UV-visible spectroscopy and H_2 -TPR. It appears that Zn incorporation inside the alumina structure, then raising the calcination temperature of the $\text{Zn}_{0.33}\text{-Al}_2\text{O}_3$ support, both increase the average size of the silver particles. As presented in Table 2, the metallic silver content (MSC) does not vary (at around 67%) when zinc is loaded inside the alumina structure, but rises when the calcination temperature of $\text{Zn}_{0.33}\text{-Al}_2\text{O}_3$ is increased from 600 °C to 800 °C (MSC = 77%) and to 1000 °C (MSC = 80%). These particles are thereby reducible at lower temperature (Table 2). Thus, the increase of the metallic silver content, together with the lowering of the reduction temperature of the silver particles, can explain the increase of CH_3CHO formation at 250 °C with $\text{Ag}/\text{Zn}_{0.33}\text{-Al}_2\text{O}_3$ C800 compared to $\text{Ag}/\text{Al}_2\text{O}_3$. Besides, UV-vis spectra deconvolution indicates that the silver state distribution is strongly affected by Zn incorporation and the temperature calcination. Fig. 14(B) shows that, except for the $\text{Ag}/\text{Zn}_{0.33}\text{-Al}_2\text{O}_3$ C1000 sample, the CH_3CHO formation at 250 °C is not catalyzed by the oxidized $\text{Ag}_n^{\delta+}$ cluster amount. These results are consistent with TEM and H_2 -TPR experiments, showing that ethanol dehydrogenation is mainly catalyzed by metallic sites. Concerning $\text{Ag}/\text{Zn}_{0.33}\text{-Al}_2\text{O}_3$ C1000, it is likely that the low surface area of the support ($S_{\text{BET}} = 65 \text{ m}^2/\text{g}$) is responsible for its low EtOH-SCR activity. Indeed, the surface area of $\text{Ag}/\text{Zn}_{0.33}\text{-Al}_2\text{O}_3$ C800 is twice higher ($S_{\text{BET}} = 117 \text{ m}^2/\text{g}$). These results show that the support sites are implicated in the EtOH dehydrogenation as well.

Finally, the superior catalytic performance of the $\text{Ag}/\text{Zn}_{0.33}\text{-Al}_2\text{O}_3$ C800 catalyst is attributed to its unique surface structure and the strong interactions between the support and the silver active phase. Ethanol dehydrogenation is mainly dependent on the metal-support interaction, as supported by other studies [82,83].

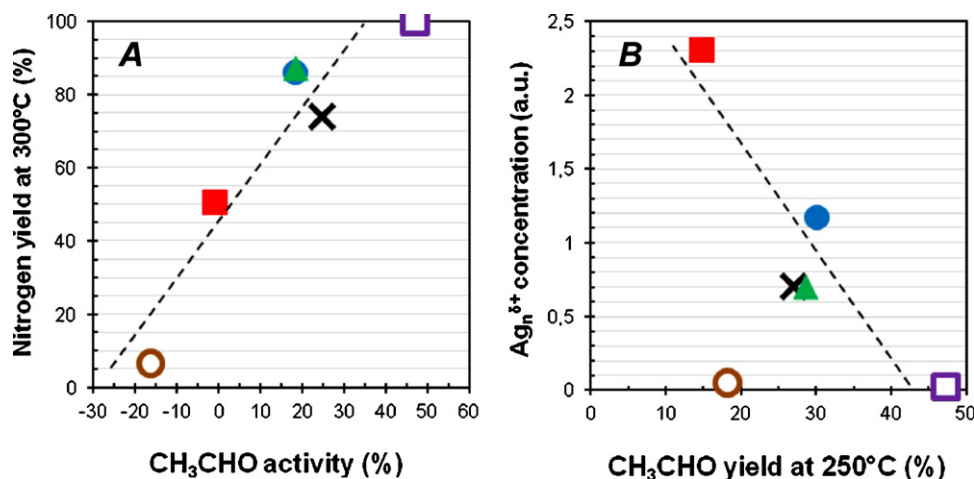


Fig. 14. Relation between (A) the CH₃CHO activity during the EtOH-SCR test and the nitrogen yield obtained at 300 °C; (B) the CH₃CHO formation at 250 °C and the relative concentration of Ag_n^{δ+} species. (x) Ag/Al₂O₃; (■) Ag/Zn_{0.1}-Al₂O₃; (●) Ag/Zn_{0.2}-Al₂O₃; (▲) Ag/Zn_{0.33}-Al₂O₃; (□) Ag/Zn_{0.33}-Al₂O₃ C800; (○) Ag/Zn_{0.33}-Al₂O₃ C1000.

4.2. Nitrogen and ammonia formation at high temperature ($T \geq 350^\circ\text{C}$)

At high temperature (i.e. $T \geq 350^\circ\text{C}$) results presented in Fig. 11(B) and Table 4 show that the obtained total NO_x conversion is concomitant with significant emission of ammonia, whatever the catalysts. For instance, the NH₃ selectivity/yield reaches 50% at 450 °C with Ag/Zn_{0.33}-Al₂O₃. To our knowledge, such emission is not highlighted in the literature. Proposed mechanisms suggest the formation of surface acetate ions or enolic surface species [38] that furthermore react with NO₂ to produce nitromethane, leading to the production of isocyanate intermediate species (reaction (1), cf. Section 1). The formation of –NCO species has been observed in numerous papers [84,85] over Ag/Al₂O₃ catalysts when high NO_x reduction efficiency is achieved. The chemistry of HNCO formation is well established [37,41] and involves hydrolysis of HNCO to form NH₃, via reaction (2). Ammonia can thereafter react with NO₂ to form ammonium nitrite (reaction (3)). Ammonium nitrite is thermally unstable above 100 °C and decomposes to form H₂O and N₂. Isocyanate ions can also react with NO₂ [37] at low temperature (e.g. below 200 °C). This reaction is however slower than that of NCO[–] with water, which leads to ammonia formation.

Besides, it was recently established that aluminum sites, with two possible coordination states (tetrahedral Al_(IV) and octahedral

Al_(VI)), greatly influence the catalytic performances and selectivity in the NO_x removal process over Ag/Al₂O₃ [36,51]. Thus, Fig. 15 reports the amount of NH₃ yield detected at 450 °C versus the pyridine coordinated at 450 °C. However, note that coordinative unsaturated sites of catalysts have been characterized by in situ IR experiments, outgassing at 450 °C. On the contrary, water added in the feed stream during the catalytic test could lead to the formation of new OH groups by dissociation on Lewis acid–base pairs. However, in this temperature range (i.e. $T \geq 350^\circ\text{C}$), it is assuming that the influence of water adsorption is weak. Firstly, the relationship between ammonia yield and the total amount of LAS is examined. Fig. 15(A) shows that NH₃ emission growth with the total LAS quantity. More specifically, strong (Al_{IV}³⁺) and weak (Al_{VI}³⁺) Lewis acid sites were identified as the origin of the –NCO spill over [29], through a transfer of the isocyanate from Al_(VI) to Al_(IV). Thibault-Starzyk et al. [51] showed that –NCO species are formed at the interface between Ag_n^{δ+} silver cluster and Al_(VI)³⁺ weak Lewis acidic sites of the alumina support. Authors showed that a Ag_n^{δ+}–CN–Al_{VI} bridge is formed first. Then, –CN– spills over the Al_{VI} center, and is further oxidized to form the isocyanate (Al_{VI})–NCO species. Yet, since ammonia formation comes from the hydrolysis of –NCO, it must as well be linked to the Al_(VI)³⁺ centers of the alumina support. In this context, the ammonia yield was thus regarded as a function of the medium Al_(VI)³⁺ Lewis acid site density (Fig. 15(B)),

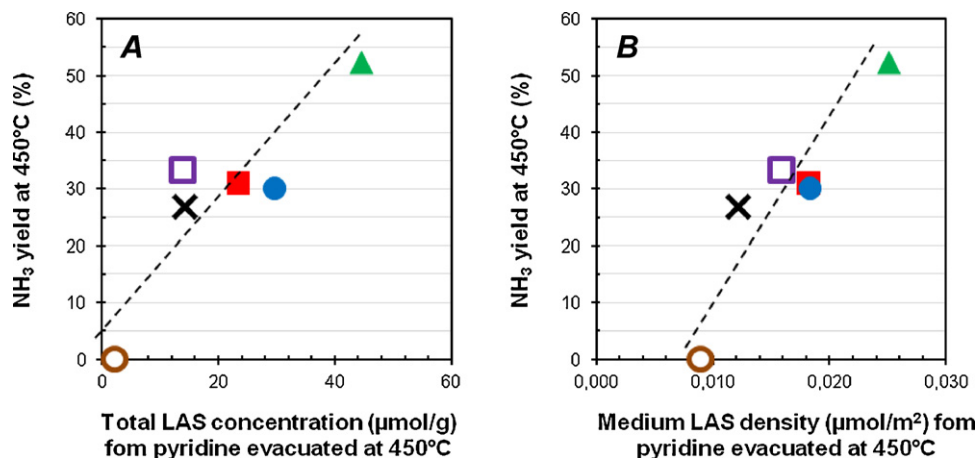
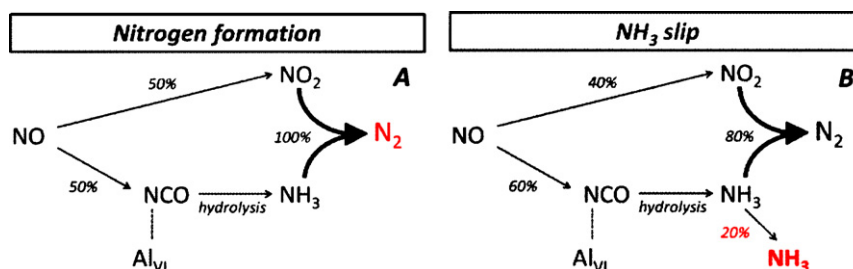


Fig. 15. Relationship between the ammonia yield at 450 °C versus pyridine coordinated at 450 °C in function of (A) the total amount of LAS (μmol g^{–1}); (B): the density of medium LAS (μmol/m²) obtained by integration of the ν_{8a} at 1617 cm^{–1}. (x) Ag/Al₂O₃; (■) Ag/Zn_{0.1}-Al₂O₃; (●) Ag/Zn_{0.2}-Al₂O₃; (▲) Ag/Zn_{0.33}-Al₂O₃; (□) Ag/Zn_{0.33}-Al₂O₃ C800; (○) Ag/Zn_{0.33}-Al₂O₃ C1000.



Scheme 1. Involvement of $\text{Al}_{(\text{VI})}^{3+}$ centers in (A) nitrogen formation by NO_2 reduction with NH_3 ; (B) NH_3 slip. (%) = percentage of converted product.

determined by integration of ν_{8a} (1617 cm^{-1}) of pyridine evacuated at 450°C (Table 1).

The increase in medium LAS density, involving the entire weak $\text{Al}_{(\text{VI})}^{3+}$ centers, results in a linearly growth of the ammonia yield. Yet ammonia formation is only observed with silver supported materials (contrary to the supports alone, cf. Table 4). So, this relation suggests a strong interaction between the silver active sites and the acidic ones located on alumina surface or zinc aluminate layer. This conclusion is in accordance with the $\text{Ag}_n^{\delta+}\text{--CN--Al}_{\text{VI}}$ bridge described by Thibault-Starzyk et al. [51], which shows that both sites are needed to form --NCO , and then ammonia.

Then, Eq. (3) denoted a stoichiometric reaction between NH_3 and NO_2 , leading to the nitrogen formation. To be selective into N_2 , introduced NO must be equally transformed into NO_2 and NH_3 . Yet, isocyanate hydrolysis reaction pathway is enhanced by a high $\text{Al}_{(\text{VI})}^{3+}$ unsaturated sites density, as illustrated in Scheme 1. It explains why when the $\text{Al}_{(\text{VI})}^{3+}$ density is too high, NH_3 slip can occur. Moreover, the higher the $\text{Al}_{(\text{VI})}^{3+}$ density, the higher the ammonia emission.

5. Conclusion

Surface and metallic properties of $\text{Ag}/\text{Zn}_x\text{--Al}_2\text{O}_3$ catalysts have been characterized, in regard with the selective catalytic reduction of NO_x with ethanol. A special attention was paid to the effect of the calcination temperature (from 600°C up to 1000°C), as well as the Zn content.

Zn incorporation into the alumina network leads to the formation of the ZnAl_2O_4 spinel structure. In parallel, variations in acidity of the resulting supports have been observed, contrarily to their basicity. Precisely, zinc addition modifies the support LAS amount and density. Metallic phase characterizations show that silver state on these materials is complex. It appears that all samples present oxidized and metallic particles, in various ratios. The metallic silver/oxidized silver species ratio is not affected by the percentage of zinc loaded into the alumina (from 0.10% to 0.33%), but increases with the calcination temperature of the support (from 600°C to 1000°C for the $\text{Zn}_{0.33}\text{--Al}_2\text{O}_3$ support). However, zinc addition leads to an increase of the silver particle mean size. Besides, different silver oxidized species have been identified whatever the support: Ag^+ ions and $\text{Ag}_n^{\delta+}$ clusters. These species are assumed, in the literature, to be involved in the SCR activity. Ag^+ ions are showed to decrease in parallel with an increase of the $\text{Ag}_n^{\delta+}$ clusters, when zinc is loaded into the alumina. The opposite phenomenon is observed when the calcination temperature of $\text{Zn}_{0.33}\text{--Al}_2\text{O}_3$ support is raised from 600°C to 1000°C .

EtOH-SCR tests demonstrate the benefit of zinc addition for NO_x conversion in nitrogen. The higher efficiency was obtained with the $\text{Ag}/\text{Zn}_{0.33}\text{--Al}_2\text{O}_3$ C800 formulation, which yields 100% N_2 at 300°C , compared to 73% for the $\text{Ag}/\text{Al}_2\text{O}_3$ reference sample. This higher performance is explained by the activation of the ethanol conversion in acetaldehyde. It is proposed that metallic silver, together with support sites, are responsible for the dehydrogenation of

ethanol into acetaldehyde. Activation of acetaldehyde formation at 250°C on $\text{Ag}/\text{Zn}_x\text{--Al}_2\text{O}_3$ C800 compared to $\text{Ag}/\text{Al}_2\text{O}_3$ must be partly correlated to its increase in the silver particles mean size. Indeed, it leads to a lowering of the maximum reduction temperature of the silver particles, from 319°C to 235°C . It was also demonstrated that the CH_3CHO activity directly impacts the N_2 yield at 300°C . The higher the CH_3CHO activity parameter, the higher the nitrogen formation at 300°C .

Finally, it has been showed that the LAS interfere in the N-products selectivity, more especially in ammonia emission. Particularly, weak LAS are identified as active sites involved in the formation of isocyanate species, which can thereafter react with NO_2 to form nitrogen. Selective conversion of NO_x into nitrogen requires an equal transformation of NO into NO_2 or --NCO species. When the LAS density is too high, the balance tends toward --NCO formation, which can react with H_2O to yield ammonia in absence of NO_x . It is proposed that the active site for --NCO formation is a silver species close to a Lewis acidic site of the support.

References

- [1] W.S. Epling, L.E. Campbell, A. Yezerets, N.W. Currier, J.E. Parks, *Catalysis Reviews – Science and Engineering* 46 (2004) 163–245.
- [2] H.L. Fang, H.F.M. DaCosta, *Applied Catalysis B: Environmental* 46 (2003) 17–34.
- [3] M. Eichelbaum, R.J. Farrauto, M.J. Castaldi, *Applied Catalysis B: Environmental* 97 (2010) 90–97.
- [4] F. Birkhold, U. Meingast, P. Wassermann, O. Deutschmann, *Applied Catalysis B: Environmental* 70 (2007) 119–127.
- [5] F.Z. Everton, *Chemical Engineering Science* 64 (2009) 1075–1084.
- [6] M. Koebel, M. Elsener, M. Kleemann, *Catalysis Today* 59 (2000) 335–345.
- [7] M. Koebel, M. Elsener, *Journal of Chromatography A* 689 (1995) 164–169.
- [8] O. Kroecher, M. Elsener, *Chemical Engineering Journal* 152 (2009) 167–176.
- [9] A. Lundstrom, B. Andersson, L. Olsson, *Chemical Engineering Journal* 150 (2009) 544–550.
- [10] G. Piazzesi, O. Kroecher, M. Elsener, A. Wokaun, *Applied Catalysis B: Environmental* 65 (2006) 55–61.
- [11] J.A. Sullivan, J.A. Doherty, *Applied Catalysis B: Environmental* 55 (2005) 185–194.
- [12] A. Grossale, I. Nova, E. Tronconi, D. Chatterjee, M. Weibel, *Topics in Catalysis* 52 (2009) 1837–1841.
- [13] J.H. Park, H.J. Park, J.H. Baik, I.S. Nam, C.H. Shin, J.H. Lee, B.K. Cho, S.H. Oh, *Journal of Catalysis* 240 (2006) 47–57.
- [14] J.A. Sullivan, O. Keane, *Applied Catalysis B: Environmental* 61 (2005) 244–252.
- [15] M. Konsolakis, I.V. Yentekakis, *Journal of Catalysis* 198 (2001) 142–150.
- [16] J. Shibata, K. Shimizu, A. Satsuma, T. Hattori, *Applied Catalysis B: Environmental* 37 (2002) 197–204.
- [17] E.F. Iliopoulou, A.P. Evdou, A.A. Lemonidou, I.A. Vasalos, *Applied Catalysis A: General* 274 (2004) 179–189.
- [18] K. Arve, F. Klingstedt, K. Eranen, J. Warna, L.E. Lindfors, D.Y. Murzin, *Chemical Engineering Journal* 107 (2005) 215–220.
- [19] I. Sobczak, M. Ziolek, M. Nowacka, *Microporous and Mesoporous Materials* 78 (2005) 103–116.
- [20] S.C. Shen, S. Kawi, *Applied Catalysis B: Environmental* 45 (2003) 63–76.
- [21] L.F. Cordoba, W.M.H. Sachtler, C.M. de Correa, *Applied Catalysis B: Environmental* 56 (2005) 269–277.
- [22] I.V. Yentekakis, V. Tellou, G. Botzoulaki, I.A. Rapakousios, *Applied Catalysis B: Environmental* 56 (2005) 229–239.
- [23] T. Maunula, J. Ahola, H. Hamada, *Applied Catalysis B: Environmental* 26 (2000) 173–192.
- [24] V. Houel, P. Millington, R. Rajaram, A. Tsolakis, *Applied Catalysis B: Environmental* 77 (2007) 29–34.

- [25] B. Sawatmongkhon, A. Tsolakis, S. Sitshebo, J. Rodriguez-Fernandez, M. Ahmadinejad, J. Collier, R.R. Rajaram, *Applied Catalysis B: Environmental* 97 (2010) 373–380.
- [26] V. Houel, P. Millington, R. Rajaram, A. Tsolakis, *Applied Catalysis B: Environmental* 73 (2007) 203–207.
- [27] T. Miyadera, *Applied Catalysis B: Environmental* 2 (1993) 199–205.
- [28] M. Luo, B. Zhu, L. Zhou, X. Yuan, *Journal of Fuel Chemistry and Technology* 24 (1996) 201–206.
- [29] J.A. Rodriguez, M. Kuhn, J. Hrbek, *Journal of Physical Chemistry* 100 (1996) 18240–18248.
- [30] N. Aoyama, K. Yoshida, A. Abe, T. Miyadera, *Catalysis Letters* 43 (1997) 249–253.
- [31] N. Bion, J. Saussey, C. Hedouin, T. Seguelong, M. Daturi, *Physical Chemistry Chemical Physics* 3 (2001) 4811–4816.
- [32] N. Bogdanchikova, F.C. Meunier, M. Avalos-Borja, J.P. Breen, A. Pestryakov, *Applied Catalysis B: Environmental* 36 (2002) 287–297.
- [33] A. Satsuma, J. Shibata, A. Wada, Y. Shinozaki, T. Hattori, *Studies in Surface Science and Catalysis* 145 (2002) 235–238.
- [34] E.M. Cordi, J.L. Falconer, *Applied Catalysis A: General* 151 (1997) 179–191.
- [35] S. Kameoka, Y. Ukisu, T. Miyadera, *Physical Chemistry Chemical Physics* 2 (2000) 367–372.
- [36] Z.M. Wang, M. Yamaguchi, I. Goto, M. Kumagai, *Physical Chemistry Chemical Physics* 2 (2000) 3007–3015.
- [37] Y.H. Yeom, M.J. Li, W.M.H. Sachtler, E. Weitz, *Journal of Catalysis* 246 (2007) 413–427.
- [38] H. He, Y.B. Yu, *Catalysis Today* 100 (2005) 37–47.
- [39] A. Obuchi, I. Kaneko, J. Oi, A. Ohi, A. Ogata, G.R. Bamwenda, S. Kushiya, *Applied Catalysis B: Environmental* 15 (1998) 37–47.
- [40] Y.B. Yu, H. He, Q.C. Feng, H.W. Gao, X. Yang, *Applied Catalysis B: Environmental* 49 (2004) 159–171.
- [41] N. Macleod, R.M. Lambert, *Chemical Communications* (2003) 1300–1301.
- [42] A. Sultana, M. Haneda, T. Fujitani, H. Hamada, *Catalysis Letters* 114 (2007) 96–102.
- [43] X. She, M. Flytzani-Stephanopoulos, *Journal of Catalysis* 237 (2006) 79–93.
- [44] P. Sazama, L. Capek, H. Drobna, Z. Sobalik, J. Dedeczek, K. Arve, B. Wichterlova, *Journal of Catalysis* 232 (2005) 302–317.
- [45] F.C. Meunier, J.P. Breen, V. Zuzaniuk, M. Olsson, J.R.H. Ross, *Journal of Catalysis* 187 (1999) 493–505.
- [46] S.T. Korhonen, A.M. Beale, M.A. Newton, B.M. Weckhuysen, *Journal of Physical Chemistry C* 115 (2011) 885–896.
- [47] M.K. Kim, P.S. Kim, J.H. Baik, I.S. Nam, B.K. Cho, S.H. Oh, *Applied Catalysis B: Environmental* 105 (2011) 1–14.
- [48] D.Y. Yoon, J.H. Park, H.C. Kang, P.S. Kim, I.S. Nam, G.K. Yeo, J.K. Kil, M.S. Cha, *Applied Catalysis B: Environmental* 101 (2011) 275–282.
- [49] V.I. Parvulescu, B. Cojocaru, V. Parvulescu, R. Richards, Z. Li, C. Cadigan, P. Granger, P. Miquel, C. Hardacre, *Journal of Catalysis* 272 (2010) 92–100.
- [50] K. Sato, T. Yoshinari, Y. Kintaichi, M. Haneda, H. Hamada, *Applied Catalysis B: Environmental* 44 (2003) 67–78.
- [51] F. Thibault-Starzyk, E. Seguin, S. Thomas, M. Daturi, H. Arnolds, D.A. King, *Science* 324 (2009) 1048–1051.
- [52] F. Can, A. Flura, X. Courtois, S. Royer, G. Blanchard, P. Marecot, D. Duprez, *Catalysis Today* 164 (2011) 474–479.
- [53] X.L. Zhang, H. He, Z.C. Ma, *Catalysis Communications* 8 (2007) 187–192.
- [54] T.E. Hoost, R.J. Kudla, K.M. Collins, M.S. Chattha, *Applied Catalysis B: Environmental* 13 (1997) 59–67.
- [55] M.C. Kung, H.H. Kung, *Topics in Catalysis* 10 (2000) 21–26.
- [56] M. Bonne, Optimisation de la synthèse de matériaux poreux de haute surface, composés d'oxydes simples (SiO_2 , TiO_2 , Al_2O_3) et d'oxydes mixtes (perovskites), pour des applications en catalyse hétérogène, Chimie Organique, minérale, industrielle, Université de Poitiers, Poitiers, 2010.
- [57] T. Sato, S. Goto, Q. Tang, S. Yin, *Journal of Materials Science* 43 (2008) 2247–2253.
- [58] S. Khabtoui, T. Chevreau, J.C. Lavalley, *Microporous Materials* 3 (1994) 133–148.
- [59] K.A. Bethke, H.H. Kung, *Journal of Catalysis* 172 (1997) 93–102.
- [60] A. Musi, P. Massiani, D. Brouri, J.M. Trichard, P. Da Costa, *Catalysis Letters* 128 (2009) 25–30.
- [63] A.N. Pestryakov, A.A. Davydov, *Journal of Electron Spectroscopy and Related Phenomena* 74 (1995) 195–199.
- [72] H. Knozinger, P. Ratnasamy, *Catalysis Reviews – Science and Engineering* 17 (1978) 31–70.
- [73] A.A. Tsyganenko, V.N. Filimonov, *Journal of Molecular Structure* 19 (1973) 579–589.
- [74] A.A. Tsyganenko, V.N. Filimonov, *Spectroscopy Letters* 13 (1980) 583–592.
- [75] F. Can, A. Travert, V. Ruaux, J.P. Gilson, F. Mauge, R. Hu, R.F. Wormsbecher, *Journal of Catalysis* 249 (2007) 79–92.
- [76] C. Morterra, G. Ghiotti, F. Boccuzzi, S. Coluccia, *Journal of Catalysis* 51 (1978) 299–313.
- [77] G. Busca, V. Lorenzelli, V.S. Escibano, R. Guidetti, *Journal of Catalysis* 131 (1991) 167–177.
- [78] J. Popovic, E. Tkalec, B. Grzeta, S. Kurajica, B. Rakvin, *American Mineralogist* 94 (2009) 771–776.
- [79] E.P. Parry, *Journal of Catalysis* 2 (1963) 371–379.
- [80] Y.H. Yeom, M.J. Li, W.M.H. Sachtler, E. Weitz, *Journal of Catalysis* 238 (2006) 100–110.
- [81] A. Le Valant, N. Bion, F. Can, D. Duprez, F. Epron, *Applied Catalysis B: Environmental* 97 (2010) 72–81.
- [82] M.S. Ghattas, *Journal of Molecular Catalysis A: Chemical* 248 (2006) 175–180.
- [83] W.-L. Dai, Y. Cao, L.-P. Ren, X.-L. Yang, J.-H. Xu, H.-X. Li, H.-Y. He, K.-N. Fan, *Journal of Catalysis* 228 (2004) 80–91.
- [84] S. Kameoka, T. Chafik, Y. Ukisu, T. Miyadera, *Catalysis Letters* 51 (1998) 11–14.
- [85] Y. Yeom, M. Li, A. Savara, W. Sachtler, E. Weitz, *Catalysis Today* 136 (2008) 55–63.